

## Mathematical modeling of cancer cell invasion of tissue: biological insight from mathematical analysis and computational simulation

Vivi Andasari · Alf Gerisch · Georgios Lolas ·  
Andrew P. South · Mark A. J. Chaplain

Received: 8 June 2010 / Revised: 30 August 2010 / Published online: 26 September 2010  
© Springer-Verlag 2010

**Abstract** The ability of cancer cells to break out of tissue compartments and invade locally gives solid tumours a defining deadly characteristic. One of the first steps of invasion is the remodelling of the surrounding tissue or extracellular matrix (ECM) and a major part of this process is the over-expression of proteolytic enzymes, such as the urokinase-type plasminogen activator (uPA) and matrix metalloproteinases (MMPs), by the cancer cells to break down ECM proteins. Degradation of the matrix enables the cancer cells to migrate through the tissue and subsequently to spread to secondary sites in the body, a process known as metastasis. In this paper we undertake an analysis of a mathematical model of cancer cell invasion of tissue, or ECM, which focuses on the role of the urokinase plasminogen activation system. The model consists of a system of five reaction-diffusion-taxis partial differential equations describing the

---

V. Andasari (✉) · M. A. J. Chaplain  
Division of Mathematics, University of Dundee, Dundee DD1 4HN, Scotland  
e-mail: vivi@maths.dundee.ac.uk

M. A. J. Chaplain  
e-mail: chaplain@maths.dundee.ac.uk

A. Gerisch  
Technische Universität Darmstadt, Fachbereich Mathematik, 64293 Darmstadt, Germany  
e-mail: gerisch@mathematik.tu-darmstadt.de

G. Lolas  
Department of Chemical Engineering, National Technical University of Athens,  
Aigaleo, Athens, Greece  
e-mail: glolas@yahoo.gr

A. P. South  
Department of Surgery and Molecular Oncology, Ninewells Hospital, University of Dundee,  
Dundee DD1 9SY, Scotland  
e-mail: a.p.south@dundee.ac.uk

interactions between cancer cells, uPA, uPA inhibitors, plasmin and the host tissue. Cancer cells react chemotactically and haptotactically to the spatio-temporal effects of the uPA system. The results obtained from computational simulations carried out on the model equations produce dynamic heterogeneous spatio-temporal solutions and using linear stability analysis we show that this is caused by a taxis-driven instability of a spatially homogeneous steady-state. Finally we consider the biological implications of the model results, draw parallels with clinical samples and laboratory based models of cancer cell invasion using three-dimensional invasion assay, and go on to discuss future development of the model.

**Keywords** Cancer invasion · uPA system · Haptotaxis · Spatio-temporal heterogeneity · Organotypic culture · Invasion index

**Mathematics Subject Classification (2000)** 92C17 · 92-08 · 92C15 · 35K57 · 65M20

## 1 Introduction

*In vivo* cancer growth is a complicated phenomenon involving many inter-related processes at many spatial and temporal scales. Solid tumour growth occurs in two distinct phases: the initial growth being referred to as the relatively harmless avascular phase and the later growth as the vascular phase. The transition from avascular growth to vascular growth depends upon the crucial process of angiogenesis and is necessary for the tumour to attain nutrients and dispose of waste products (Folkman 1974, 1976). To achieve vascularisation, tumour cells secrete a diffusible substance known as tumour angiogenesis factor (TAF) into the surrounding tissue (Folkman and Klagsbrun 1987). This has the effect of stimulating nearby capillary blood vessels to grow towards and penetrate the tumour, re-supplying the tumour with vital nutrient. Invasion and metastasis can now take place.

Mathematical modelling of the various phases of solid tumour growth has itself been developing and expanding over the years. For comprehensive reviews of the modelling in this area, see the books (Adam and Bellomo 1996; Preziosi 2003; Bellomo and De Angelis 2008), the articles (Bellomo et al. 2003; Szymańska 2003; Matzavinos et al. 2004; Matzavinos and Chaplain 2004), and the review papers (Araujo and McElwain 2004; Mantzaris et al. 2004; Lowengrub et al. 2010). Until relatively recently, perhaps less attention has been devoted to the mathematical modelling of cancer invasion. However, over the last 15 years or so models of cancer invasion have started to appear in the research literature (Gatenby 1995; Gatenby and Gawlinski 1996; Orme and Chaplain 1996; Perumpanani et al. 1996, 1998; Anderson et al. 2000; Byrne et al. 2001; Turner and Sherratt 2002; Anderson 2005; Chaplain and Lolas 2005, 2006; Frieboes et al. 2006; Hillen 2006; Gerisch and Chaplain 2008; Ramis-Conde et al. 2008; Anderson et al. 2009; Poplawski et al. 2009; Szymańska et al. 2009; Painter 2009; Painter et al. 2010).

Cancer cell invasion is a very complex process. Understanding its many aspects is facilitated by an understanding of the interactions of the key components of invasion,

such as the urokinase plasminogen activation (uPA) system for matrix degradation. In this paper we focus on the uPA system as given in [Chaplain and Lolas \(2005\)](#) and discuss its role in tissue invasion, tumour heterogeneity and its biological and clinical implications.

In the model under consideration, the interactions of cancer cells and  $l$  chemicals are described by a system of  $l + 1$  reaction-diffusion-taxis equations of the form

$$\partial_t n = D_n \Delta n - \nabla \cdot \left( n \sum_{j=1}^l p_j(n, \mathbf{c}) \nabla c_j \right) + f(n, \mathbf{c}), \tag{1a}$$

$$(t, \mathbf{x}) \in (0, T] \times \Omega.$$

$$\partial_t \mathbf{c} = \mathbf{D} \Delta \mathbf{c} + \mathbf{g}(n, \mathbf{c}), \tag{1b}$$

where we denote the time ( $t$ ) and space ( $\mathbf{x}$ ) dependent concentrations of the chemical species by the vector valued function  $\mathbf{c}(t, \mathbf{x})$  and the density of the cancer cells by  $n(t, \mathbf{x})$ ,

$$\mathbf{c} : [0, T] \times \bar{\Omega} \rightarrow \mathbb{R}^l \quad \text{and} \quad n : [0, T] \times \bar{\Omega} \rightarrow \mathbb{R}.$$

Here,  $\Omega \subset \mathbb{R}^d$ ,  $d = 1$  or  $d = 2$ , is a bounded domain and  $[0, T]$  is the time interval of interest. Furthermore, the cancer cell random motility coefficient  $D_n \geq 0$  and the diagonal matrix  $\mathbf{D} \geq 0$  of chemical diffusion coefficients, the taxis functions  $p_j$ ,  $j = 1, \dots, l$ , associated with each chemical  $c_j$ , as well as the reaction terms  $f$  and  $\mathbf{g}$  are given. The temporal derivative is denoted by  $\partial_t$ , the spatial gradient operator by  $\nabla$ , and the Laplace operator by  $\Delta$ . The partial differential equation (PDE) system (1) is supplied with appropriate initial and boundary conditions.

The remaining sections of the paper are as follows. In Sect. 2, we provide specific details of the process of extracellular matrix degradation during tissue invasion and describe the major features of the uPA system. Next, the mathematical model of the uPA system is presented in Sect. 3. A linear stability analysis of the positive, spatially uniform steady state of the model system is given in Sect. 4. This analysis gives rise to the observation that the model allows for taxis-driven instability of that steady state. We also carry out a parameter sensitivity analysis for parameters that are related with increased malignancy of the cancer cells. In Sect. 5, we present computational simulations of the model confirming the results obtained from the linear stability analysis. Here we also comment on appropriate numerical schemes for the simulation of the model equations. Finally, in Sect. 6, we conclude this paper with a discussion of the results obtained in comparison with experimental data from *in vitro* invasion assays. A brief discussion of ongoing and future work is also given.

In summary, the key results of this paper are: (1) comprehensive computational simulations of our mathematical model of cancer invasion and the observation of interesting spatio-temporal irregular patterns; (2) the linking of these patterns to results of a linear stability analysis of unique positive uniform steady states of the system, and, (3) a comparison of the computational simulations with experimental results and identification of weakness of the model for future work.

## 2 Cancer invasion: the uPA system and its role in ECM proteolysis

The prognosis of a cancer is primarily dependent on its ability to invade and metastasise, and a crucial component of these processes is the degradation of extracellular matrix (ECM). A major constituent of ECM are proteins and their directed degradation by cellular enzymes (proteolytic enzymes or proteases for short) is called proteolysis.

Many steps that occur during tumour invasion and the formation of metastasis (as well as in a number of distinct physiological events in the healthy organism) require the regulated turnover of ECM macromolecules. It is now widely believed that the breakdown of these barriers is catalysed by proteases released from the invading cancer cells. Most of these proteases belong to one of two general classes: matrix metalloproteases (MMPs) (Parsons et al. 1997; Pepper 2001) or serine proteases (Andreasen et al. 1997, 2000). Proteases give cancers their defining deadly characteristic—the ability of malignant cells to break out of tissue compartments.

The enzymatic system we will focus on in this paper is the urokinase plasminogen activation system (uPA system) which consists of:

- uPA, the urokinase plasminogen activator,
- uPAR, the urokinase plasminogen activator receptor,
- plasmin, the matrix degrading enzyme,
- VN, the ECM protein vitronectin, and
- PAI-1, the plasminogen activator inhibitor type-1.

A schematic diagram of the key interactions of the system is given in Fig. 1.

uPA is an extracellular serine protease. Cells secrete its enzymatically inactive form pro-uPA into the extracellular space. pro-uPA is activated by plasmin to its active form uPA. In the model below, we do not distinguish between pro-uPA and uPA, which both bind to uPA receptors (uPAR) located on the cell membrane. Two major functional domains make up the uPA molecule: the protease domain and the

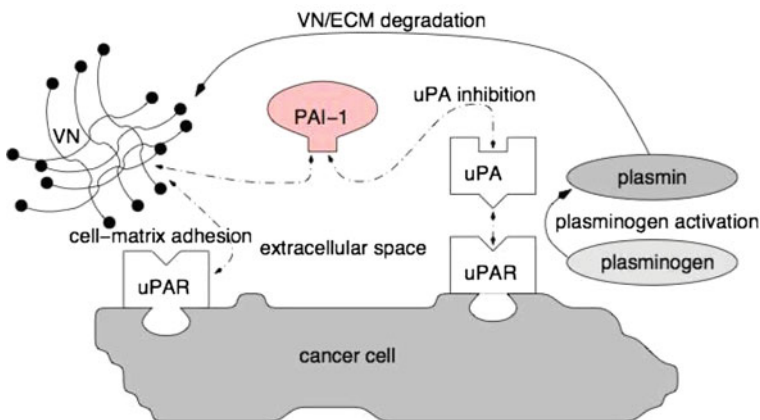


**Fig. 1** A schematic diagram of the uPA system showing its main components and their interactions

growth factor domain (not discussed here). The protease moiety in uPAR-bound uPA activates the pro-enzyme plasminogen to its active form plasmin. Plasminogen is a ubiquitous protein produced mainly in the liver and present in blood and the ECM. Plasmin itself is a broadly acting serine protease that, either directly or through the activation of other proteases, catalyses the breakdown of many of the known ECM and basement membrane molecules, such as vitronectin (VN), fibronectin, fibrin, laminin, thrombospondin, and collagens. Therefore, to maintain tissue homeostasis and to avoid unrestrained tissue damage, the process of plasminogen activation in a healthy organism is strictly controlled through the availability of uPA, localised activation, and interaction with specific inhibitors (PAIs). One of these inhibitors, PAI-1, is believed to be the most abundant fast-acting inhibitor of uPA *in vivo* (Andreasen et al. 1997, 2000). In other words, for cells to protect themselves they must secrete a surplus of inhibitors to guarantee restraint of pericellular proteolysis. Indeed secreted uPA is often associated with PAI-1 and remains inactive. PAI-1 has a high affinity to the ECM constituent VN and VN-bound PAI-1 remains in an active conformation for prolonged periods of time.

These facts suggest that the five molecules uPA, PAI-1, plasmin, uPAR and VN constitute the core of an integrated dynamical system which allows spatial and temporal rearrangements of its components at cell surfaces during cell migration and invasion. Moreover, it has become clear that this system has a multi-functional role in cancer biology. The system seems to function not only in cancer cell migration and invasion, but also in remodelling of the tissue surrounding the cancer cells, which may contribute decisively to the overall process of metastasis.

### 3 The mathematical model of the uPA system and cancer cell invasion

In this section we present the mathematical model of the uPA system and cancer cell invasion of tissue. The model explicitly considers the production of plasmin and the interactions between cancer cells (with uPAR located on their surface), uPA, PAI-1, plasmin, and the ECM component VN. In the model we assume an unrestricted supply of plasminogen. Furthermore, we assume a fixed average number of uPARs located on each cancer cells surface. This implies that the concentration of uPAR is proportional to the cancer cell density and we do not explicitly model the evolution of uPAR. We denote the cancer cell density by  $n(t, \mathbf{x})$ , the uPA concentration by  $u(t, \mathbf{x})$ , the PAI-1 concentration by  $p(t, \mathbf{x})$ , the plasmin concentration by  $m(t, \mathbf{x})$ , and the VN concentration by  $v(t, \mathbf{x})$ . We briefly describe the main interactions between all the variables before writing the system of equations. A fuller description may be found in Chaplain and Lolas (2005).

#### 3.1 Cancer cells

The dominating factors governing cancer cell migration are random motion, chemotaxis due to uPA and PAI-1 as well as haptotaxis due to VN and other ECM components. Besides migration, cancer cell proliferation is also included in the model in the form of a logistic growth law.

### 3.2 Extracellular matrix

It is known that ECM does not diffuse and therefore we omit any diffusion term (or other “migration” terms) from its model equation.

Furthermore, based on the experimental evidence that uPA activates plasminogen to its cancer cell-surface associated form plasmin, which in turn catalyses the breakdown of VN (and other ECM molecules), we model the fact that plasmin degrades VN upon contact at a (degradation) rate  $\delta$ . The inhibitor PAI-1 also binds to VN and in this way inhibits VN from binding to cell-surface receptors (such as uPAR and/or integrins) and promoting its own production through the regulation of cell–matrix-associated signal transduction pathways. This effect is accounted for by the degradation term  $-\phi_{22}vp$ . Furthermore, it is assumed that the latter process is reversed by PAI-1 binding to uPA and the production term  $\phi_{21}up$  is added to the model. Finally, a logistic growth term accounts for the remodelling of the ECM by the cells present in the tissue.

### 3.3 Urokinase plasminogen activator

The spatio-temporal evolution of the concentration of uPA is assumed to occur through diffusion, cancer cells acting as sources, while its binding to PAI-1 and uPAR dominates its removal from the system.

### 3.4 Plasminogen activator inhibitor-1

The conservation equation for the concentration of PAI-1 is similar to that of uPA. Thus, we assume it diffuses, with its production being a result of plasmin activation and its neutralisation in the system occurs by its binding to VN and to uPA.

### 3.5 Plasmin

In examining spatio-temporal evolution of the plasmin concentration, we assume that it also diffuses. Furthermore, we assume that binding of uPA to uPAR provides the cell surface with a potential proteolytic activity via activation and cell-surface co-localisation of plasminogen and thus leads to plasmin formation. Additionally, the binding of PAI-1 to VN indirectly results in the binding of uPA to uPAR and therefore in enhanced plasmin formation. Finally, the term  $-\phi_{54}m$  models the deactivation of plasmin either by degradation or by the action of the plasmin inhibitor  $\alpha_2$ -antiplasmin.

The mathematical model depicting the interactions between all variables described above, in its non-dimensionalised form, is given by

$$\partial_t n = \underbrace{D_n \Delta n}_{\text{random motility}} - \nabla \cdot \left[ \underbrace{\chi_u n \nabla u}_{\text{uPA-chemo}} + \underbrace{\chi_p n \nabla p}_{\text{PAI-1-chemo}} + \underbrace{\chi_v n \nabla v}_{\text{VN-hapto}} \right] + \underbrace{\mu_1 n(1-n)}_{\text{proliferation}}, \quad (2a)$$

$$\partial_t v = - \underbrace{\delta v m}_{\text{degradation}} + \underbrace{\phi_{21} u p}_{\text{uPA/PAI-1}} - \underbrace{\phi_{22} v p}_{\text{PAI-1/VN}} + \underbrace{\mu_2 v(1-v)}_{\text{remodelling}}, \quad (2b)$$

$$\partial_t u = \underbrace{D_u \Delta u}_{\text{diffusion}} - \underbrace{\phi_{31} pu}_{\text{uPA/PAI-1}} - \underbrace{\phi_{33} nu}_{\text{uPA/uPAR}} + \underbrace{\alpha_{31} n}_{\text{production}}, \tag{2c}$$

$$\partial_t p = \underbrace{D_p \Delta p}_{\text{diffusion}} - \underbrace{\phi_{41} pu}_{\text{PAI-1/uPA}} - \underbrace{\phi_{42} pv}_{\text{PAI-1/VN}} + \underbrace{\alpha_{41} m}_{\text{production}}, \tag{2d}$$

$$\partial_t m = \underbrace{D_m \Delta m}_{\text{diffusion}} + \underbrace{\phi_{52} pv}_{\text{PAI-1/VN}} + \underbrace{\phi_{53} un}_{\text{uPA/uPAR}} - \underbrace{\phi_{54} m}_{\text{degradation}}. \tag{2e}$$

These model equations coincide with those given in [Chaplain and Lolas \(2005\)](#) (Eq. 10), except for some minor details irrelevant for the model predictions. The non-dimensional system was obtained by rescaling distance with the maximum distance of the cancer cells at this early stage of invasion  $L := 0.1\text{cm}$ , time with  $\tau := L^2 D^{-1}$ , where  $D := 10^{-6}\text{cm}^2 \text{s}^{-1}$  is a representative chemical diffusion coefficient. The dependent variables  $v, u, p, m$  are rescaled with appropriate reference concentration values  $v_0, u_0, p_0, m_0$  in the nanomolar range,  $1\text{nM} \equiv 10^{-9}\text{mol/l}$  taken from [Chaplain and Lolas \(2005\)](#), while the reference cancer cell density  $n_0$  is taken from [Gerisch and Chaplain \(2008\)](#). The full set of scaling parameters is given by

$$L = 0.1\text{cm}, \quad \tau = \frac{L^2}{D} = 10^4\text{s}, \quad n_0 = 6.7 \times 10^7 \text{ cell cm}^{-3}, \quad v_0 = 1\text{nM}, \\ u_0 = 1\text{nM}, \quad p_0 = 1\text{nM}, \quad m_0 = 0.1\text{nM}.$$

In this work we consider a default set of model parameters referred to as *parameter set*  $\mathcal{P}$ . The majority of the values of the parameters are taken from [Chaplain and Lolas \(2005\)](#), except for the values of the new parameter  $\phi_{54}$ , and also for parameters  $\mu_1$  and  $\mu_2$  which are cell proliferation and ECM remodelling terms, respectively. We consider here the rate of ECM remodelling slower than cell proliferation ([Perentes et al. 2009](#)). The values of the non-dimensional parameter set  $\mathcal{P}$  are given by

$$D_n = 3.5 \cdot 10^{-4}, \quad D_u = 2.5 \cdot 10^{-3}, \quad D_p = 3.5 \cdot 10^{-3}, \quad D_m = 4.91 \cdot 10^{-3}, \\ \chi_u = 3.05 \cdot 10^{-2}, \quad \chi_p = 3.75 \cdot 10^{-2}, \quad \chi_v = 2.85 \cdot 10^{-2}, \quad \mu_1 = 0.25, \\ \delta = 8.15, \quad \phi_{21} = 0.75, \quad \phi_{22} = 0.55, \quad \mu_2 = 0.15, \\ \phi_{31} = 0.75, \quad \phi_{33} = 0.3, \quad \alpha_{31} = 0.215, \\ \phi_{41} = 0.75, \quad \phi_{42} = 0.55, \quad \alpha_{41} = 0.5, \\ \phi_{52} = 0.11, \quad \phi_{53} = 0.75, \quad \phi_{54} = 0.5.$$

[we note that the dimensional values of the parameters can be recovered using the scalings detailed above e.g.  $D_n$  (dimensional)  $= 3.5 \cdot 10^{-4} \times 10^{-6}\text{cm}^2\text{s}^{-1} = 3.5 \cdot 10^{-10}\text{cm}^2\text{s}^{-1}$ . Full details can be found in [Chaplain and Lolas \(2005\)](#) and [Gerisch and Chaplain \(2008\)](#)].

We consider system (2) to hold for times  $t \in (0, T]$  and on a bounded spatial domain  $\Omega \subset \mathbb{R}^d$ , for  $d = 1$  or  $d = 2$ , representing a region of tissue. We use two different cases of domains, each parameterised by a positive parameter  $M$ : the one-dimensional domain  $\Omega_1 := (-M, M) \subset \mathbb{R}$  and the two-dimensional square domain

$\Omega_2 := (-M, M) \times (-M, M) \subset \mathbb{R}^2$ . For reasons of symmetry, in our computational simulations in Sect. 5 we take  $\Omega_1 := (0, M) \subset \mathbb{R}$  for the one-dimensional domain and  $\Omega_2 := (0, M) \times (0, M) \subset \mathbb{R}^2$  for the two-dimensional square domain.

System (2) must be closed by appropriate initial and boundary conditions for each of the dependent variables. For the two cases of domains we use different initial conditions for cancer cell density and ECM/VN concentration. For the one-dimensional domain case we assume that initially there is a cluster of cancer cells already present at  $\mathbf{x} = \mathbf{0}$  and that they have penetrated a short distance into the extracellular matrix, while the remaining space is occupied by the matrix alone. Additionally, we assume that the uPA protease as well as the PAI-1 inhibitor initial concentration are proportional to the initial cancer cell density while the plasmin protease is not yet produced by the cancer cells. Specifically, the initial conditions for system (2) in one-dimensional spatial domain are taken to be

$$\begin{aligned} n(0, \mathbf{x}) &= \exp(-|\mathbf{x}|^2 \varepsilon^{-1}), \\ v(0, \mathbf{x}) &= 1 - \frac{1}{2} \exp(-|\mathbf{x}|^2 \varepsilon^{-1}), \\ u(0, \mathbf{x}) &= \frac{1}{2} \exp(-|\mathbf{x}|^2 \varepsilon^{-1}), \quad \text{for } \mathbf{x} \in \bar{\Omega}_1, \\ p(0, \mathbf{x}) &= \frac{1}{20} \exp(-|\mathbf{x}|^2 \varepsilon^{-1}), \\ m(0, \mathbf{x}) &= 0, \end{aligned} \tag{3}$$

where throughout the paper we have taken  $\varepsilon = 0.01$ .

For the two-dimensional square domain case, the cancer cells are initially placed to form a strip along the top of the domain. The strip of cancer cells takes about 20% of the domain and is at a uniform initial density of 1, while the ECM/VN concentration uniformly occupies the rest of 80% of the domain also at initial concentration 1. The uPA, PAI-1, and plasmin at  $t = 0$  follow those in Eq. 3, i.e.,  $u(0, \mathbf{x}) = 0.5n(0, \mathbf{x})$ ,  $p(0, \mathbf{x}) = 0.05n(0, \mathbf{x})$ , and  $m(0, \mathbf{x}) = 0$ .

We assume that cancer cells, and as a consequence uPA, PAI-1 and plasmin, remain within the domain of tissue under consideration and therefore zero-flux boundary conditions are imposed on  $\partial\Omega$ , the boundary of  $\Omega$ . For the ECM density,  $v(t, \mathbf{x})$  satisfies an ordinary differential equation (ODE) and so no boundary conditions can be prescribed.

## 4 Linear stability analysis

### 4.1 Positive, spatially uniform steady states

We first write the solution components of the model (2) as a vector  $\mathbf{w}(t, \mathbf{x})$

$$\mathbf{w}(t, \mathbf{x}) := (n(t, \mathbf{x}), v(t, \mathbf{x}), u(t, \mathbf{x}), p(t, \mathbf{x}), m(t, \mathbf{x})).$$

We are interested in the existence of spatially uniform steady states  $\mathbf{w}^* = (n^*, v^*, u^*, p^*, m^*)$  of the system (2). From Eq. 2a we see that  $n^* = 0$  or  $n^* = 1$ . The

first case leads to non-positive steady states and is not discussed. So in the following we investigate the case  $n^* = 1$ . In the case of the parameter set  $\mathcal{P}$ , the one positive and unique steady state  $\mathbf{w}^*$  is given by

$$\mathbf{w}^* := (n^*, v^*, u^*, p^*, m^*) \approx (1, 0.047, 0.222, 0.889, 0.343). \tag{4}$$

(Indeed, we note that for all parameter sets used in the paper, it was verified using both *Mathematica* and *Maple* that a unique positive steady state existed.) This steady state is linearly stable which can be seen by evaluating the Jacobian matrix  $J_R(\mathbf{w})$  of the reaction terms, given by

$$J_R(\mathbf{w}) = \begin{pmatrix} \mu_1(1 - 2n) & 0 & 0 & 0 & 0 \\ 0 & -\delta m - \phi_{22}p + \mu_2(1 - 2v) & \phi_{21}p & \phi_{21}u - \phi_{22}v & -\delta v \\ -\phi_{33}u + \alpha_{31} & 0 & -\phi_{31}p - \phi_{33}n & -\phi_{31}u & 0 \\ 0 & -\phi_{42}p & -\phi_{41}p & -\phi_{41}u - \phi_{42}v & \alpha_{41} \\ \phi_{53}u & \phi_{52}p & \phi_{53}n & \phi_{52}v & -\phi_{54} \end{pmatrix} \tag{5}$$

at  $\mathbf{w}^*$  and observing that its eigenvalues have a maximum real part of  $\approx -0.24$ .

### 4.2 Dispersion curves and taxis-driven instability

Here we investigate the linear stability of system (2) in the vicinity of a spatially uniform steady state  $\mathbf{w}^*$ . To this end, we write the solutions  $\mathbf{w}(t, \mathbf{x})$  of this system as small perturbations of  $\mathbf{w}^*$ ,

$$\mathbf{w}(t, \mathbf{x}) := \mathbf{w}^* + \varepsilon \tilde{\mathbf{w}}(t, \mathbf{x}),$$

where  $\varepsilon > 0$  is small and  $\tilde{\mathbf{w}}(t, \mathbf{x})$  is bounded. We consider the PDE systems for  $\mathbf{x} \in (-M, M)^d$  with periodic boundary conditions and assume that the perturbations can be written as  $d$ -dimensional Fourier series for all  $t \geq 0$ , that is

$$\tilde{\mathbf{w}}(t, \mathbf{x}) = \sum_{\mathbf{k} \in \mathbb{Z}^d} \mathbf{a}_{\mathbf{k}}(t) \exp(i\mathbf{k}\pi M^{-1} \cdot \mathbf{x})$$

with coefficient functions  $\mathbf{a}_{\mathbf{k}} : [0, T] \rightarrow \mathbb{C}^5$  for each  $\mathbf{k} \in \mathbb{Z}^d$ . In the following we use the notation  $\tilde{\mathbf{k}} \equiv \mathbf{k}\pi M^{-1}$ . This allows for the visualisation of dispersion relations independent of the domain size parameter  $M$ .

Linearising system (2) around a spatially uniform steady state  $\mathbf{w}^*$  leads, upon dropping terms of order  $\varepsilon^2$  or higher and dividing by  $\varepsilon$ , to

$$\frac{\partial \tilde{\mathbf{w}}}{\partial t} = J_T(\mathbf{w}^*)\Delta \tilde{\mathbf{w}} + J_R(\mathbf{w}^*)\tilde{\mathbf{w}}. \tag{6}$$

Here, the reaction Jacobian  $J_R(\mathbf{w}^*)$  is given by (5). Furthermore, the transport Jacobian  $J_T(\mathbf{w}^*)$ , accounting for diffusion and taxis, is

$$J_T(\mathbf{w}^*) = \begin{pmatrix} D_n - \chi_v n^* - \chi_u n^* - \chi_p n^* & 0 & 0 & 0 & 0 \\ 0 & 0 & 0 & 0 & 0 \\ 0 & 0 & D_u & 0 & 0 \\ 0 & 0 & 0 & D_p & 0 \\ 0 & 0 & 0 & 0 & D_m \end{pmatrix}. \tag{7}$$

Inserting the Fourier series representation of  $\tilde{\mathbf{w}}$  into (6) leads to

$$\sum_{\mathbf{k} \in \mathbb{Z}^d} \left[ \dot{\mathbf{a}}_{\mathbf{k}}(t) + \left( \|\tilde{\mathbf{k}}\|_2^2 J_T(\mathbf{w}^*) - J_R(\mathbf{w}^*) \right) \mathbf{a}_{\mathbf{k}}(t) \right] \exp(i\tilde{\mathbf{k}} \cdot \mathbf{x}) = 0.$$

Furthermore, expanding the initial perturbation  $\tilde{\mathbf{w}}(0, \mathbf{x})$  of the PDE system in a Fourier series defines coefficients  $\mathbf{a}_{\mathbf{k},0}$  via

$$\tilde{\mathbf{w}}(0, \mathbf{x}) = \sum_{\mathbf{k} \in \mathbb{Z}^d} \mathbf{a}_{\mathbf{k},0} \exp(i\tilde{\mathbf{k}} \cdot \mathbf{x}).$$

Both relations imply that the Fourier coefficients  $\mathbf{a}_{\mathbf{k}}(t)$  satisfy the linear ODE systems

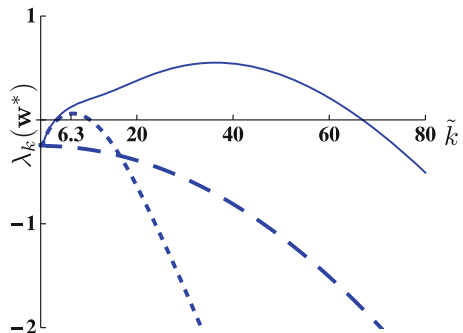
$$\dot{\mathbf{a}}_{\mathbf{k}}(t) = - \left( \|\tilde{\mathbf{k}}\|_2^2 J_T(\mathbf{w}^*) - J_R(\mathbf{w}^*) \right) \mathbf{a}_{\mathbf{k}}(t), \quad \mathbf{a}_{\mathbf{k}}(0) = \mathbf{a}_{\mathbf{k},0}.$$

A growth of  $\mathbf{a}_{\mathbf{k}}(t)$  then indicates a growth of the perturbation due to mode  $\exp(i\tilde{\mathbf{k}} \cdot \mathbf{x})$  whereas this perturbation is damped away with time if  $\mathbf{a}_{\mathbf{k}}(t) \rightarrow 0$  for  $t \rightarrow \infty$ . Which type of behaviour takes place for a given perturbation mode is determined by the linear stability of the zero steady state of the above ODE. In more detail, a perturbation due to mode  $\exp(i\tilde{\mathbf{k}} \cdot \mathbf{x})$  grows if

$$\lambda_{\mathbf{k}}(\mathbf{w}^*) := \max\{\text{real part of the eigenvalues of } J_R(\mathbf{w}^*) - \|\tilde{\mathbf{k}}\|_2^2 J_T(\mathbf{w}^*)\} > 0.$$

If  $\lambda_{\mathbf{k}}(\mathbf{w}^*) < 0$  then the perturbation is damped away. (The case  $\lambda_{\mathbf{k}}(\mathbf{w}^*) = 0$  can be treated as usual for linear ODE systems and leads to either growth or damping.)

**Fig. 2** Plots of the dispersion relations for the unique positive, spatially uniform steady state  $\mathbf{w}^*$  of system (2) with (1) parameter set  $\mathcal{P}$  (solid line); (2) with parameter set  $\mathcal{P}$  but all taxis coefficients set to zero (large dashed line), and (3) with parameter set  $\mathcal{P}$  but the cell random motility coefficient increased to  $D_n = 0.00425$  (small dashed line)



We are interested in deciding whether there exist non-trivial perturbation modes  $\exp(i\tilde{\mathbf{k}} \cdot \mathbf{x})$  which grow with time, i.e. destabilise the linearly stable fixed point  $\mathbf{w}^*$  of the reaction system. To this end, we plot for the 1D case ( $d = 1, \tilde{\mathbf{k}} = \tilde{k}$ ) and a given spatially uniform steady state  $\mathbf{w}^*$  the quantity  $\lambda_k(\mathbf{w}^*)$  against the (domain size scaled) wave number  $\tilde{k}$ . This gives the so-called *dispersion relation*. For the parameter set  $\mathcal{P}$  and the variations of it, these dispersion relations for system (2) are given in Fig. 2. For parameter set  $\mathcal{P}$  (see the solid line in Fig. 2) we observe that there is a range of  $\tilde{k}$ -values for which  $\lambda_k(\mathbf{w}^*)$  is positive and hence the corresponding perturbations are growing in time. This means that the unique positive, spatially uniform steady state  $\mathbf{w}^*$ , which is linearly stable for the reaction system itself, is destabilised due to the transport terms (diffusion and taxis). Furthermore, setting all taxis coefficients in parameter set  $\mathcal{P}$  to zero, there exist no values  $\tilde{k} \in [0, 80]$  for which  $\lambda_k(\mathbf{w}^*) > 0$  (large dashed line in Fig. 2). This observation implies that the destabilisation of the steady state  $\mathbf{w}^*$  in system (2) is taxis-driven. To see the effect of varying cell random motility coefficient, increasing  $D_n$  more than ten times higher, that is to  $D_n = 0.00425$ ,

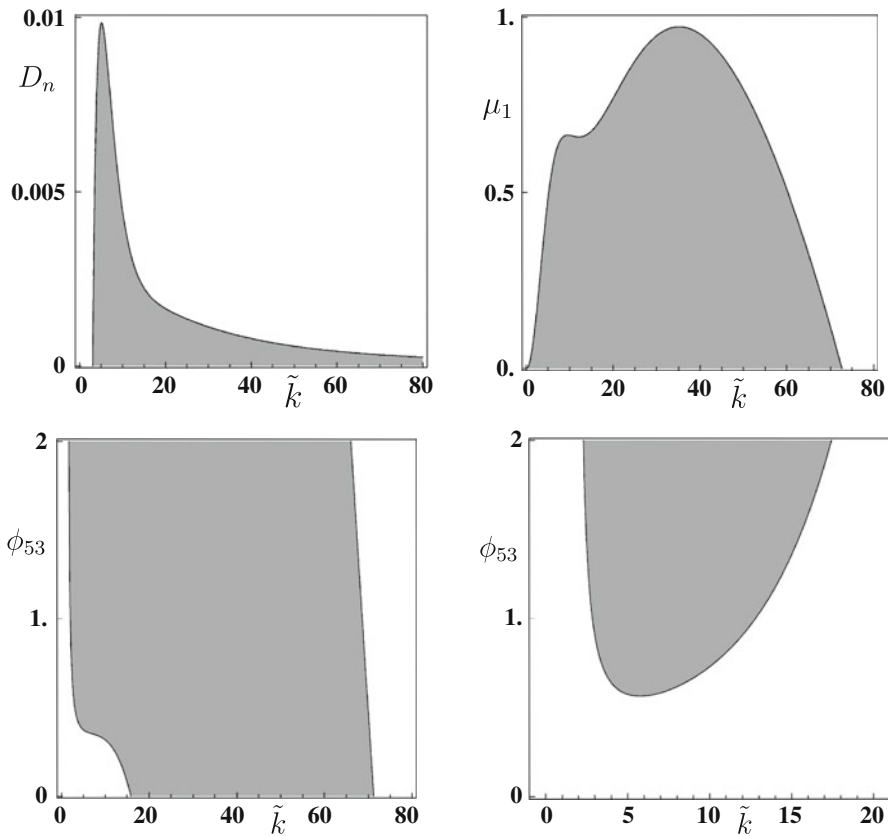


**Fig. 3** Dispersion relation of system (2) with parameters taken from set  $\mathcal{P}$  and (1)  $D_n$  varying in  $[0, 0.01]$  (top left), (2)  $\mu_1$  varying in  $[0, 1]$  (top right), (3)  $\phi_{53}$  varying in  $[0, 2]$  (bottom left), and (4)  $\phi_{53}$  varying in  $[0, 2]$  with  $D_n = 0.00425$  (bottom right) for their respective unique positive, spatially uniform steady states. The grey area indicates the  $\tilde{k}$ -values for which  $\lambda_k(\mathbf{w}^*) > 0$

decreases the range of  $\tilde{k}$ -values for positive  $\lambda_k(\mathbf{w}^*)$  (small dashed line in Fig. 2). The influence of varying cell random motility towards stability of the system is explained further in Fig. 3.

It is of interest to see how the range of  $k$ -values, for which perturbations grow, changes if key parameters of the model are modified. One such parameter is the random motility of the cancer cells,  $D_n$ . We again take the parameter set  $\mathcal{P}$  but now vary parameter  $D_n$  in the range  $[0, 0.01]$ . For each value of  $D_n$  we compute the set of  $\tilde{k}$ -values for which  $\lambda_k(\mathbf{w}^*) > 0$ . The grey area in Fig. 3, top left, visualises this set (with  $\tilde{k}$  in the range  $[0, 80]$ ). We observe that up to a maximum value of  $D_n$  there are always some values  $\tilde{k}$  with  $\lambda_k(\mathbf{w}^*) > 0$ . For decreasing cancer cell random motility  $D_n$ , the range of such  $\tilde{k}$ -values increases. This implies that increased cell random motility has a smoothing effect and leads to damping of, in particular, high frequency perturbations.

Besides the random motility coefficient  $D_n$  of the cancer cells, there are two other key parameters in the model: the proliferation rate  $\mu_1$  of cancer cells and the rate  $\phi_{53}$  of plasmin production due to uPA/uPAR binding. Varying  $\mu_1 \in [0, 1]$  but keeping parameter set  $\mathcal{P}$  otherwise unchanged, leads to the dispersion relations as shown in Fig. 3, top right plot. Here we observe that increasing cell proliferation leads to less and less amplified modes and hence eventually to the damping of all perturbations. Varying  $\phi_{53} \in [0, 2]$  and keeping all other parameters as in set  $\mathcal{P}$  gives no stability area for  $\tilde{k}$  within the range  $[15, 70]$ , (see bottom left Fig. 3). If the cancer cell random motility is increased to  $D_n = 0.00425$  and all other parameters as in set  $\mathcal{P}$ , this leads to the dispersion relations as shown in Fig. 3, bottom right plot. It tells us that at lower values of  $\phi_{53}$  with  $D_n = 0.00425$ , there are no  $\tilde{k}$ -values for which  $\lambda_k(\mathbf{w}^*) > 0$ ; all perturbations are damped. But as  $\phi_{53}$  is increased the grey area that determines instability starts to appear and the range of frequency perturbations becomes bigger at higher values of  $\phi_{53}$ .

## 5 Computational simulation results

In this section we present computational simulation results for the model (2), together with the initial conditions and zero-flux boundary conditions, given in Sect. 3. The parameters are taken from parameter set  $\mathcal{P}$  unless otherwise stated. These simulations firstly show the typical behaviour of the model solutions and, secondly, illustrate the theoretical results on taxis-driven instability as obtained in Sect. 4. The majority of the simulations presented are in a one-dimensional spatial domain, Sect. 5.2. However, we also perform two-dimensional simulations, where the results are compared with experimental data taken from an organotypic gel culture system quantifying squamous cell carcinoma invasion. We begin with a few comments on the numerical method employed in obtaining the simulation results.

### 5.1 Numerical technique

All simulation results are obtained with a custom-made code for the numerical solution of reaction-diffusion-taxis systems, see Gerisch and Chaplain (2006) and the

references therein. The code is based on the method of lines. The approach makes use of a finite volumes discretisation in space which employs, for the taxis term, a higher-order, upwind-biased discretisation with nonlinear limiter function. This dedicated treatment of the taxis terms ensures, in general, second-order accuracy of the spatial discretisation and leads to a large positive ODE system, the MOL-ODE system. Here positive means that the exact and unique solution of the ODE system with arbitrary non-negative initial data remains non-negative for all later times. Conditions which ensure this property of an ODE system are, for instance, given in Horváth (1998). We note that negative solution values are often the result of unphysical oscillations near steep fronts in the solution when the taxis terms of the PDE problem are discretised in a standard way, e.g., by central finite differences. These negative values feed back into the reaction kinetics of the system which becomes unstable and we observe a subsequent blow-up of the numerical solution within a short time. So the approach taken here does not lead to negative solution values in the exact solution of the MOL-ODE and all the problems which go with them. This particularly desirable property is achieved automatically by the spatial discretisation by locally introducing just the amount of numerical diffusion which is required to ensure the property of positivity. No user intervention is needed. With these measures taken, the code also allows for reliable computations also in the case of zero cell random motility, i.e.,  $D_n = 0$ .

After the discretisation in space a large ODE system is obtained which needs to be solved numerically. In particular, simulations of 2D problems lead to a very large dimension of the MOL-ODE system and suitable numerical schemes have to be employed. Due to the stiffness of the equations, the method selected must be implicit for computational efficiency. We have opted here for using the linearly-implicit Runge–Kutta method ROWMAP (Weiner et al. 1997). ROWMAP is designed for the efficient numerical solution of stiff initial value problems of large ODE systems. One of its particular strengths is that it requires a subroutine for the evaluation of the right-hand side of the ODE only; no explicit subroutine for the evaluation of the Jacobian matrix is required. The linear systems in the stages of the method are then solved using a multiple Arnoldi process (Weiner et al. 1997). The automatic time-step selection based on a local error control further increases the efficiency and reliability of the method.

## 5.2 Computational simulation results in 1D

The simulations in this section are obtained with the custom-made finite volume code, see Sect. 5.1. We use an equidistant covering of the spatial domain with finite volumes of length  $1/100$ . For the time integration we prescribe an absolute and relative tolerance of  $10^{-6}$  (variable time step sizes). Numerical convergence tests have shown that these choices of discretisation parameters are appropriate for the problems at hand and give sufficiently accurate solutions. We ran all simulations up to a final time  $t = 500$  unless indicated otherwise. This corresponds to a real time span of about 58 days. We have performed simulations on the domain  $\Omega = (-10, 10)$  with zero-flux as well as with periodic boundary conditions. The results are qualitatively and quantitatively similar and also similar to the results obtained with  $\Omega = (0, 10)$  and zero-flux

boundary conditions. In particular the same conclusions can be drawn. In the interest of a clearer presentation we show simulation results obtained with  $\Omega = (0, 10)$  (and  $\Omega = (0, 15)$  for certain simulations) and zero-flux boundary conditions only.

Figure 4 captures the dynamic heterogeneity of cancer cell density that evolves over time by interacting with components of the uPA system. Initially, at  $t = 0$ , we assume a cluster of cancer cells are already present and they have penetrated a small area in the extracellular matrix. By  $t = 75$  ( $\sim 8.5$  days), several clusters of cancer cells that are composed of the primary tumour occupied half of the domain.

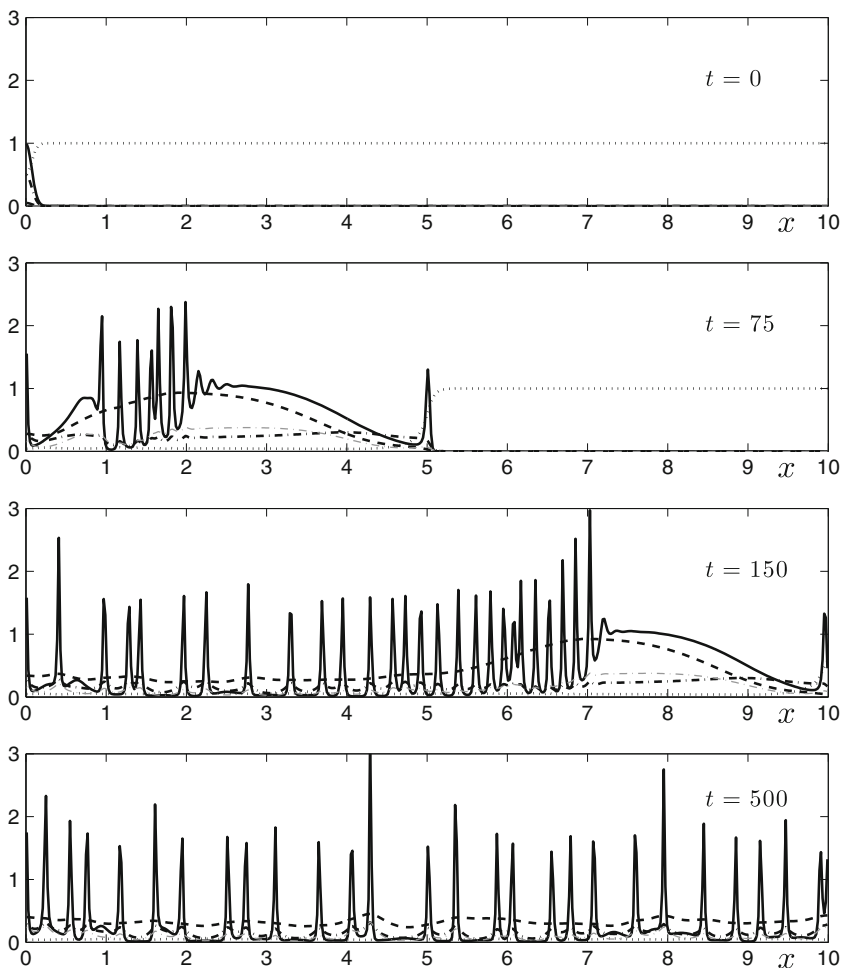


**Fig. 4** Sequence of profiles showing the spatio-temporal evolution of cancer cells  $n$  (solid black line) invading the ECM  $v$  (dotted black line) along with the other components of the model: uPA protease concentration  $u$  (dash-dotted black line), PAI-1 concentration  $p$  (dashed black line), and plasmin concentration  $m$  (dash-dotted grey thin line) for model (2) with parameter set  $\mathcal{P}$  at dimensionless times  $t = 0$ ,  $t = 75$ ,  $t = 150$ , and  $t = 500$

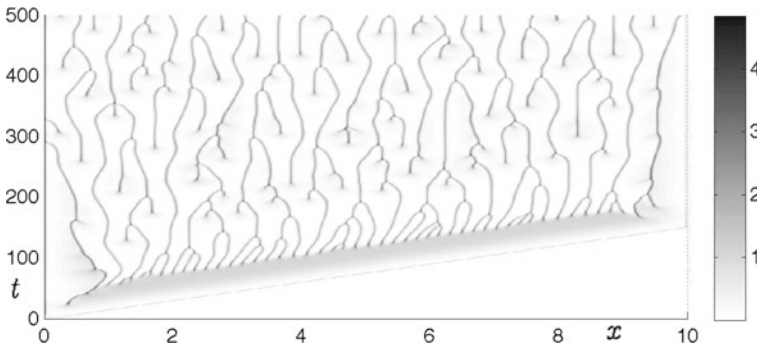


**Fig. 5** Plots showing the spatio-temporal evolution of the cancer cell density  $n$  for model (2) with parameter set  $\mathcal{P}$

At  $t = 150$  ( $\sim 17.5$  days) cancer cells have invaded the remaining of the extracellular matrix.

The spatio-temporal dynamic heterogeneity of the cancer cell density over time can also be appreciated from the plot shown in Fig. 5. The solutions are as expected from the linear stability analysis carried out in the previous section and also in line with the results obtained by Chaplain and Lolas (2005). We note that for parameter set  $\mathcal{P}$  the spatially uniform, positive steady state  $\mathbf{w}^*$  is unstable (due to the taxis, as previously shown). The initial data given by (3) allow the spread of the cancer cells into the domain in a “wave-like” manner. Of course in this case (i.e., with parameter set  $\mathcal{P}$ ) no travelling wave exists since the underlying steady state has been destabilised. We note that these results show a spatio-temporal pattern that is very similar to previous simulation results obtained by Wang and Hillen (2007) in a simpler chemotaxis system where a volume-filling term was included in a Keller–Segel model. This approach employed a “squeezing probability” with nonzero cell kinetics that resulted in merging and emerging local peaks. More recently, Hillen and Painter (2009) also obtained a similar pattern of merging and emerging peaks in one of their chemotaxis models incorporating logistic growth for the cell kinetics.

It is useful to compare certain features of these simulations with other simulations where a travelling wave does exist e.g., (furthest) distance travelled into the domain at a given point in time—see, for example, Fig. 6. In the case of parameter set  $\mathcal{P}$  we note that any initial data that can be considered a perturbation of the steady state will evolve into the observed spatio-temporal heterogeneity.

### 5.2.1 Effect of varying the parameter $D_n$

During the growth of a solid tumour, over time the cancer cells become more malignant through increased mutations. One important phenotypic consequence of this is that the cancer cells become more motile. This can be reflected in the model by increasing the parameter  $D_n$ . In Fig. 6, we show the solution profiles of all five solution components of model (2) at the fixed time point  $t = 70$  for four different values of  $D_n$ . As can be seen from the figure plots, increasing the cancer cell random motility parameter

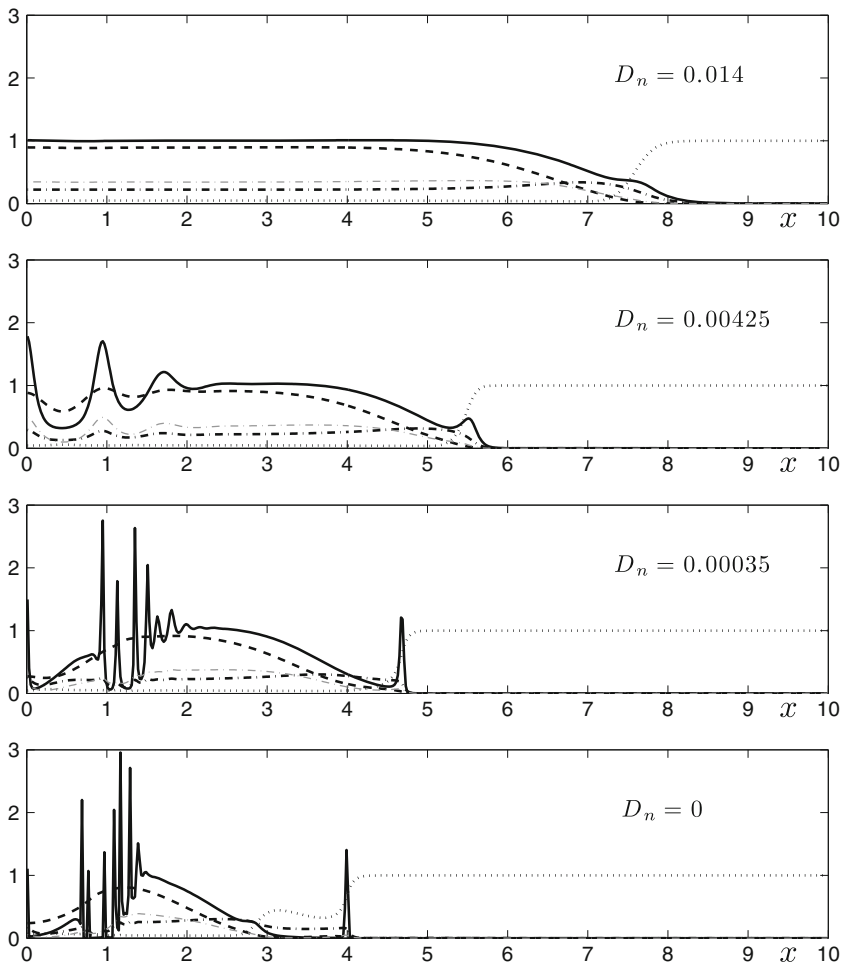


**Fig. 6** Plots showing the profiles of all variables obtained from numerical solutions of model (2) at time  $t = 70$  with Neumann BCs with parameter set  $\mathcal{P}$  but varying cell random motility coefficient  $D_n$ . Shown are the cell density  $n$  (solid black line), the ECM density  $v$  (dotted black line), the uPA concentration  $u$  (dash-dotted black line), the PAI-1 concentration  $p$  (dashed black line), and the plasmin concentration  $m$  (dash-dotted grey thin line). With increasing  $D_n$ , the profiles lose heterogeneity and eventually take on a travelling-wave-like solution

$D_n$  leads to smoother solution profiles with less steep “wave” fronts. The increased speed of propagation of the leading edge of the invasive front with increasing  $D_n$  is also obvious *i.e.* the higher the value of  $D_n$ , the faster into the tissue (ECM) the cancer cells penetrate.

In Fig. 7 we show the evolution of the cancer cell density  $n$  over time. In the top and middle plot  $D_n$  has a value of 0.014 and 0.00425, respectively, *i.e.*, increased with respect to its base value in parameter set  $\mathcal{P}$ . In the bottom plot, we have set the cell random motility to zero. Recall that the corresponding plot for  $D_n$  as given in  $\mathcal{P}$  is shown in Fig. 5.

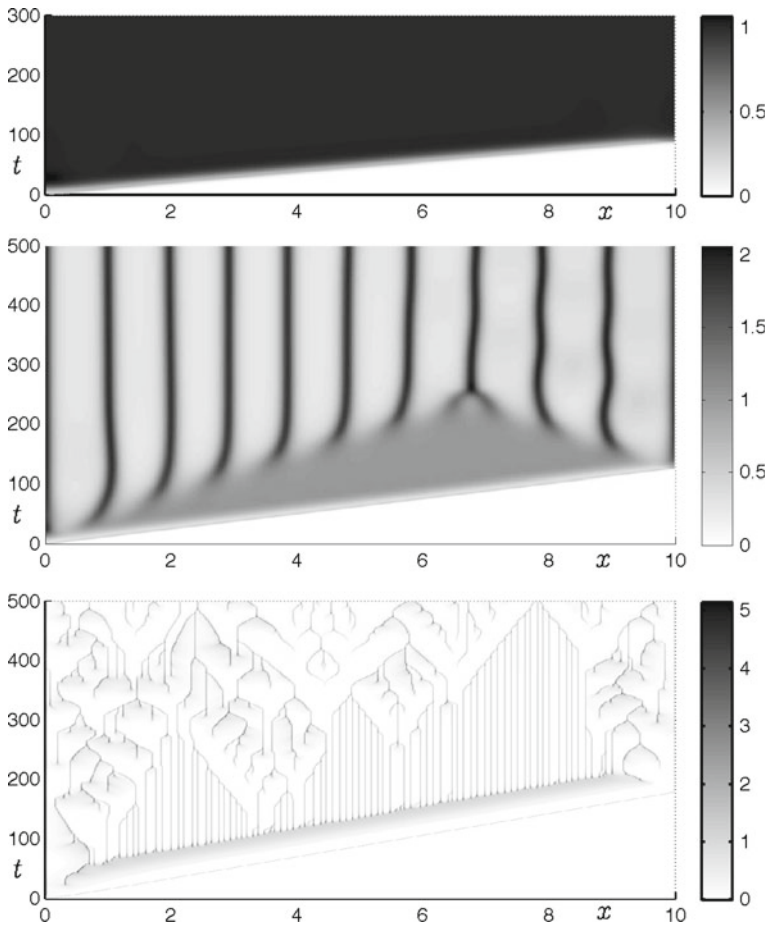


**Fig. 7** Plots showing the spatio-temporal evolution of the cancer cell density  $n$  for model (2) with parameter set  $\mathcal{P}$  and a cancer cell random motility coefficient of (1)  $D_n = 0.014$  (top); (2)  $D_n = 0.00425$  (middle) and (3)  $D_n = 0$  (bottom). For  $D_n = 0.014$ , the solution is shown up to a final time  $t = 300$  when the spatially homogeneous steady state has been reached and continues to persist. For  $D_n = 0.00425$  and  $D_n = 0$ , the solution is shown up to a final time  $t = 500$

From the top plot in Fig. 7, i.e., with  $D_n = 0.014$ , we observe a travelling wave like solution converging to the homogeneous steady state of the system. Decreasing  $D_n$  to a value of 0.00425, we observe that the solution approaches a spatially heterogeneous steady state. When the value of  $D_n = 0.00035$  is used, as given in parameter set  $\mathcal{P}$ , see Fig. 5, then a strong and persistent emerging and merging behaviour is present and no steady state is attained. This type of behaviour is even more pronounced for the case  $D_n = 0$ , as can be seen from the bottom plot of Fig. 7. We also note that the speed of propagation of the “invading wave” decreases with decreasing  $D_n$ .

The range of spatio-temporal behaviour described above may be explained by referring to the stability/instability diagrams presented in Fig. 3 (top left). For smaller  $D_n$  values more and more Fourier modes, in particular ones with higher frequencies,

are growing with time, i.e., are excited. More precisely, for  $D_n = 0.014$  all perturbations of the corresponding spatially homogeneous steady state are damped since this steady state is stable. According to the initial condition chosen, we obtain a travelling wave solution leading to the stable homogeneous steady state of the system. For  $D_n = 0.00425$ , we observe, for large times, a pattern of equally spaced peaks in the domain  $(0, 10)$ . This is the case of the onset of instability, which is a transition from a heterogeneous solution to travelling wave solution. This transition case is reminiscent of the cosine wave  $\cos(20\pi/10 \cdot x)$ . By examining the appropriate dispersion relation in Fig. 2, small dashed line, we note that the dominating mode is the one with  $\tilde{k} \approx 6.3$ , which corresponds, for  $M = 10$ , to  $k = 20$  and hence nicely explains the observed behaviour, i.e., the initial data evolves to a spatially heterogeneous steady state. For  $D_n = 0.00035$ , the dispersion relation given in Fig. 2, solid line, shows a wide range of excited modes. We observe a much more heterogeneous solution and no steady state is reached. An analysis of the relation between the number of excited modes and the observed heterogeneous solution has been provided by Aida et al. (2006). Such a refined analysis has not been attempted for the model under study in this paper. Nevertheless, the numerical results strongly suggest that an increased number of unstable modes leads to a stronger heterogeneity in the solution.

### 5.2.2 Effect of varying the parameter $\phi_{53}$

As was noted in the previous subsection, during the growth of a solid tumour, over time, the cancer cells become more malignant through increased mutations. Another important phenotypic consequence of this is that the cancer cells secrete more matrix degrading enzymes. We reflect this here in our model by increasing the parameter  $\phi_{53}$  of model (2) which prescribes the rate of plasmin production due to uPA/uPAR binding (a similar effect is achieved by varying the parameter  $\alpha_{31}$ ). To avoid the numerical effects of boundaries, we performed the simulations in the domain  $(0, 15)$ .

To see the effect of varying the parameter  $\phi_{53}$  on the evolution of the cancer cell density, initially, at  $t = 0$ , we set the value  $\phi_{53} = 0.1$ . This low level of production rate of plasmin is kept until just before  $t = 300$ , after which we increase the value of  $\phi_{53}$  smoothly to its default value 0.75 (via a smooth step-function) for the rest of the simulation. The corresponding spatio-temporal evolution of the cell density is shown in the top plot of Fig. 8. We note that the linear stability analysis carried out in Sect. 4 (and corresponding dispersion relations) indicates the changes to be expected by varying  $\phi_{53}$  while keeping other parameters as in parameter set  $\mathcal{P}$  and seen in the bottom left plot of Fig. 3.

The cancer cell density evolves from the initial data and begins to invade the ECM. Between  $t = 100$  and  $t = 200$  we can see equally spaced peaks of cancer cell density appearing in the wake of the invasive front (this corresponds with the prediction of the dispersion relation from the linear stability analysis). At around  $t = 300$  (and all subsequent times) we note that the cancer cell density in the wake of the invading front is now highly heterogeneous. Again this computational result confirms the prediction from the dispersion relation, since now  $\phi_{53} = 0.75$ . We also note a change in the speed of the invasive front when the value of  $\phi_{53}$  is increased from low (0.1) to high (0.75). At lower values of  $\phi_{53}$  the speed of the invasive front is faster than that at higher values

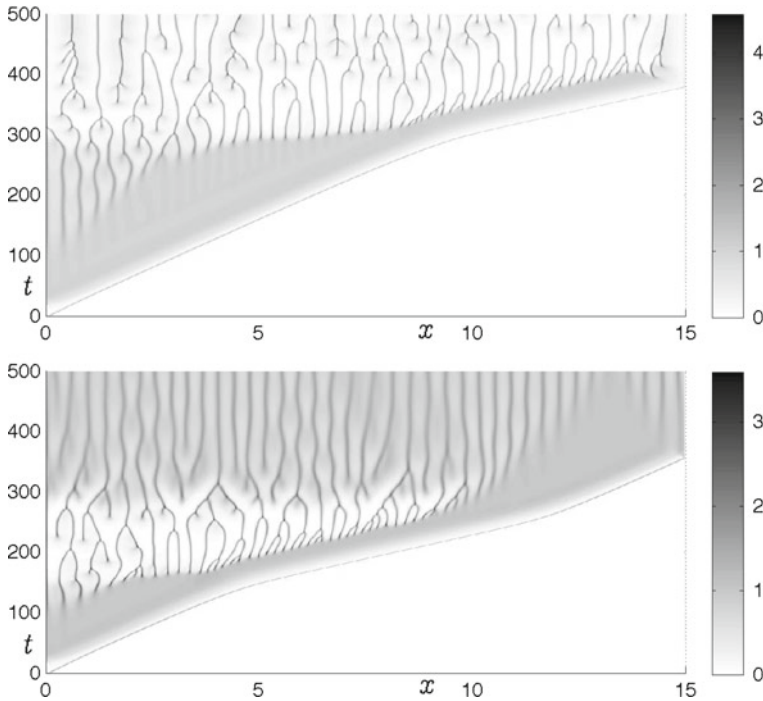


**Fig. 8** Plots showing the spatio-temporal evolution of the cancer cell density  $n$  for model (2) with parameter set  $\mathcal{P}$  in the domain  $(0,15)$ . (1) *Top plot* the parameter  $\phi_{53}$  is increased from 0.1 to 0.75 around  $t = 300$ . (2) *Bottom plot* the parameter  $\phi_{53}$  is increased from 0.1 to 0.75 around  $t = 150$  and then decreased down to 0.1 again at around  $t = 250$

of  $\phi_{53}$ . The change in the invasive speed occurs around the switching time of  $t = 300$  and can clearly be seen in the top plot of Fig. 8.

In the bottom plot of Fig. 8, the initial value of  $\phi_{53} = 0.1$  is increased smoothly around  $t = 150$  until it reaches the default value 0.75 (as prescribed by the parameter set  $\mathcal{P}$ ). After  $t = 250$  the value of  $\phi_{53}$  is then smoothly reduced back to 0.1. The figure shows the corresponding change in the nature of the cancer cell density profile. The change of the speed of the invasive front from high to low and back to high again (for the appropriate values of  $\phi_{53}$ ) is also observed here.

To see the effects of higher cell random motility in varying  $\phi_{53}$ , we performed simulations with  $D_n$  increased to 0.00425. The results are shown in Fig. 9. With the smaller values of parameter  $\phi_{53}$ , in the top plot, we see an initial travelling wave solution evolving. At around  $t = 40$ , we smoothly increase the value of  $\phi_{53}$  to its default value 0.75, where it stays for the remainder of the simulation. From the linear stability analysis, we would expect the underlying spatially homogeneous steady-state to be destabilised and this is indeed what is observed with eventually a final profile the same as that shown in Fig. 7 (middle) being attained. This process is then reversed by reducing the value of  $\phi_{53}$  smoothly back to 0.01 at around  $t = 180$ . The resulting solution is visualised in Fig. 9 (bottom). From the linear stability analysis, we would expect the spatially homogeneous steady state to have been re-stabilised and this is

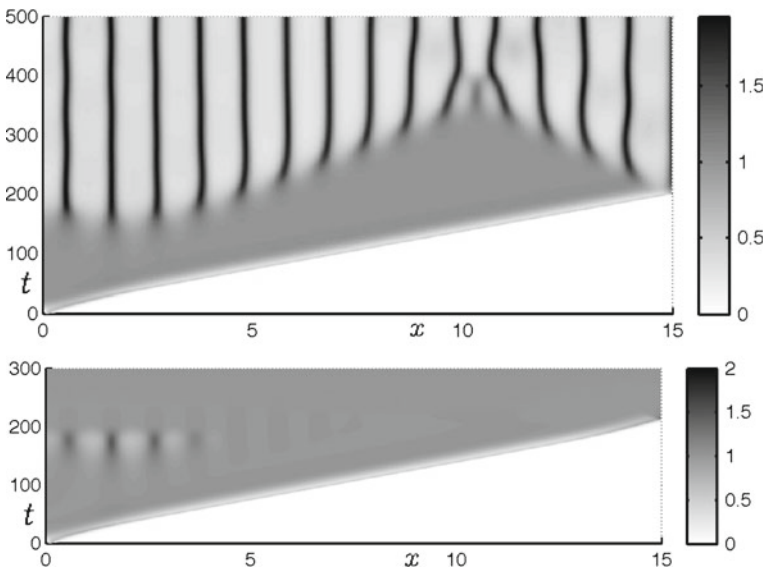


**Fig. 9** Plots showing the spatio-temporal evolution of the cancer cell density  $n$  for model (2) with parameter set  $\mathcal{P}$  and  $D_n = 0.00425$  in domain  $(0, 15)$ . In these plots, the parameter  $\phi_{53}$  is (1) increased from 0.01 to 0.75 around  $t = 40$  (top) and (2) then decreased down to 0.01 again at around  $t = 180$  (bottom)

indeed what we observe from the figure. In this case, locally in time and space we see growing perturbations shortly after the switching time  $t = 40$ . These then decay when  $\phi_{53}$  is reduced again and have disappeared immediately after  $t = 180$ , leaving a smooth travelling wave profile behind, which drives the solution to its steady state. These simulations confirm the dispersal relation curve shown in the bottom right plot of Fig. 3.

### 5.2.3 Effect of varying the parameter $\mu_1$

Similar computational experiments to the previous sub-section can be carried out by varying the cell proliferation parameter  $\mu_1$ . An increase in the cancer cell proliferation rate is yet another important phenotypic consequence of increased malignancy. In Fig. 10 we show the evolution of the cancer cell density  $n$  when  $\mu_1$  is changed with time (otherwise parameter set  $\mathcal{P}$  is used). Initially, we use  $\mu_1 = 1.0$ , i.e. above the threshold for the destabilisation of the steady state, see Fig. 3 (middle), and then decrease its value smoothly to  $\mu_1 = 0.25$ , its default value, around  $t = 100$ . Accordingly, we observe at first a travelling wave of cancer cells invading the domain. This is followed, after  $t = 100$ , by the appearance of cancer cell density heterogeneity in the wake of the wave front. The spatio-temporal structure of these solutions would persist for increasing time (not shown) if  $\mu_1$  were not changed again. Instead, at around  $t = 180$ , the value of  $\mu_1$  is increased to  $\mu_1 = 1.0$  again, leading to a (re-)stabilisation of the steady state. Correspondingly, we observe that the peaks in the cell density are damped away quickly and the solution becomes homogeneous again.

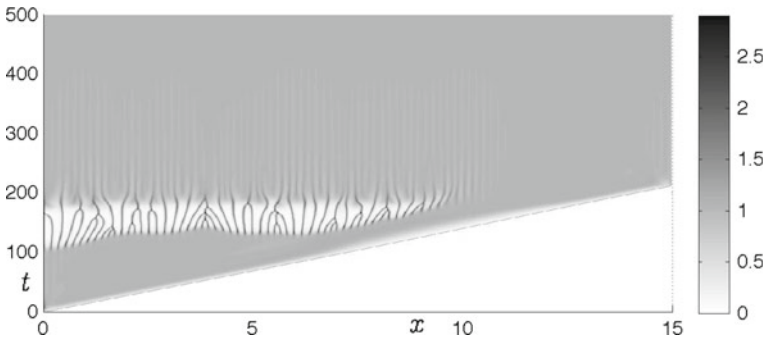


**Fig. 10** Plot showing the spatio-temporal evolution of the cancer cell density  $n$  for model (2) with parameter set  $\mathcal{P}$ . The parameter  $\mu_1$  is decreased from 1.0 to 0.25 around  $t = 100$  and then increased back to 1.0 at around  $t = 180$

5.2.4 Simulation results for modified proliferation terms

The interactions between cancer cells and the ECM due to cell movement and proliferation and ECM remodelling result in competition for physical space between the cancer cells and the ECM. Since it is considered more realistic biologically and in order to take the effect into account, in this section we modify the proliferation term of cancer cells and remodelling term of the ECM in (2) obeying the spatial restrictions. The equations for cancer cells and the ECM now become

$$\partial_t n = \underbrace{D_n \Delta n}_{\text{random motility}} - \nabla \cdot \left[ \underbrace{\chi_u n \nabla u}_{\text{uPA-chemo}} + \underbrace{\chi_p n \nabla p}_{\text{PAI-1-chemo}} + \underbrace{\chi_v n \nabla v}_{\text{VN-hapto}} \right] + \underbrace{\mu_1 n(1 - n - v)}_{\text{proliferation}}, \tag{8a}$$

$$\partial_t v = - \underbrace{\delta v m}_{\text{degradation}} + \underbrace{\phi_{21} u p}_{\text{uPA/PAI-1}} - \underbrace{\phi_{22} v p}_{\text{PAI-1/VN}} + \underbrace{\mu_2(1 - n - v)}_{\text{remodelling}}, \tag{8b}$$

subject to the boundary and initial conditions given by (3). The modified proliferation terms model the competition for space between cancer cells and the ECM. The cancer cells will grow as long as there is enough space available. The same effect applies to the ECM, where if the space is limited the ECM then will remodel back to a normal, healthy level of density. This functional form is called volume filling and it acts to prevent overcrowding among the cells and matrix. This has been considered in work by Hillen and Painter (2001); Painter and Hillen (2002). The use of these functional forms of cell proliferation and matrix remodelling specifically in cancer invasion modelling has been considered previously by Gerisch and Chaplain (2008). We note that the matrix remodelling term here is slightly different to that used in Eq. 2b. However, both are qualitatively similar in the sense that, in the absence of cancer cells (i.e. normal conditions), the ECM will tend to a steady-state value of 1. We have also carried out extensive simulations using both remodelling terms and the precise form does not make any significant difference to the results.

The simulations of the modified system is shown in Fig. 11. We observe similar dynamics as in the previous section. However, comparing solutions in Fig. 11 with solutions in Fig. 4 we see, for example, that in Fig. 4, at  $t = 75$  ( $\sim 8.5$  days) the

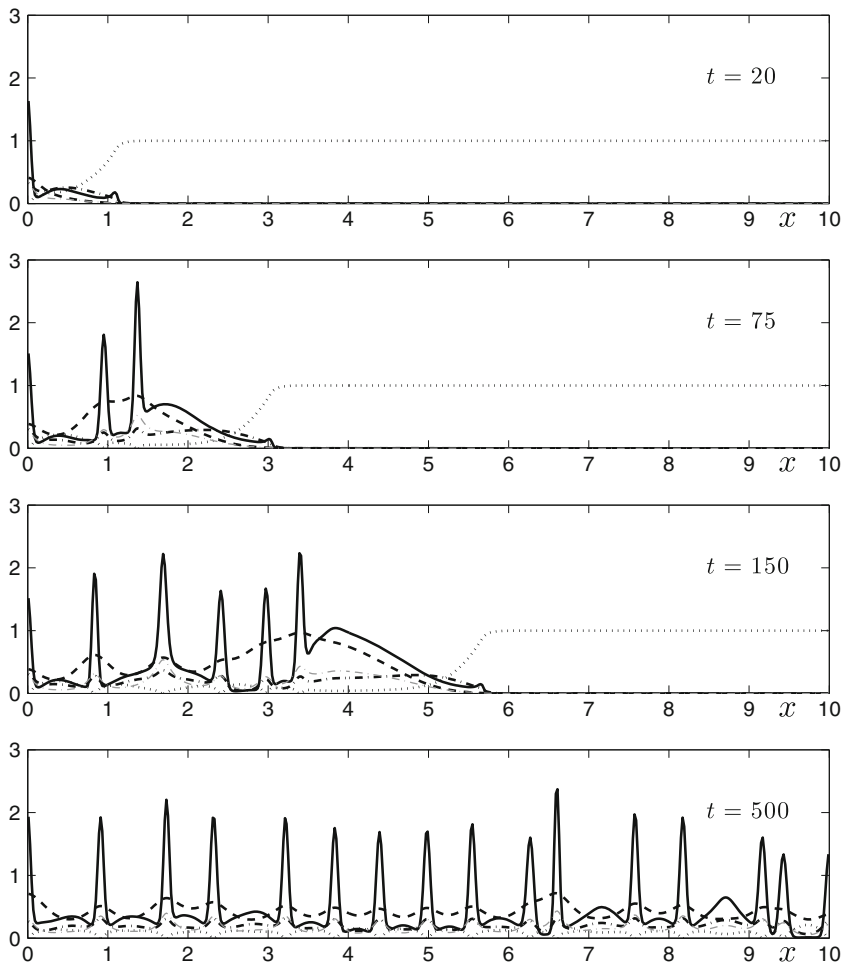


**Fig. 11** Plots showing the spatio-temporal evolution of the cancer cell density  $n$  for model (2) with modified proliferation and remodelling terms (8) on domain  $(0, 10)$  with Neumann BCs

cancer cells have already migrated through half of the domain, while in Fig. 11 they have migrated appreciably less.

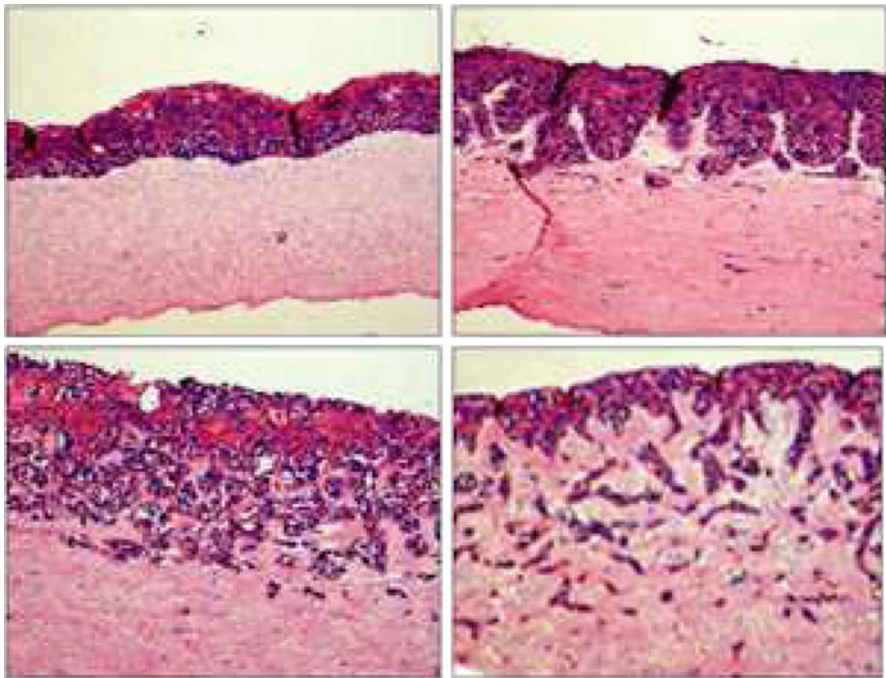
### 5.3 Computational simulation results in 2D

In this section we present computational simulation results of our model (2) with parameter set  $\mathcal{P}$  on a two-dimensional square domain with finite volumes of length  $1/50$  for each side of the domain. One of the reasons for doing this was to qualitatively compare our simulation results with experimental data obtained from an *in vitro* organotypic culture model developed to examine the invasiveness of cancer cells into a collagen:matrigel gel (Nyström et al. 2005; Martins et al. 2009). Although our model

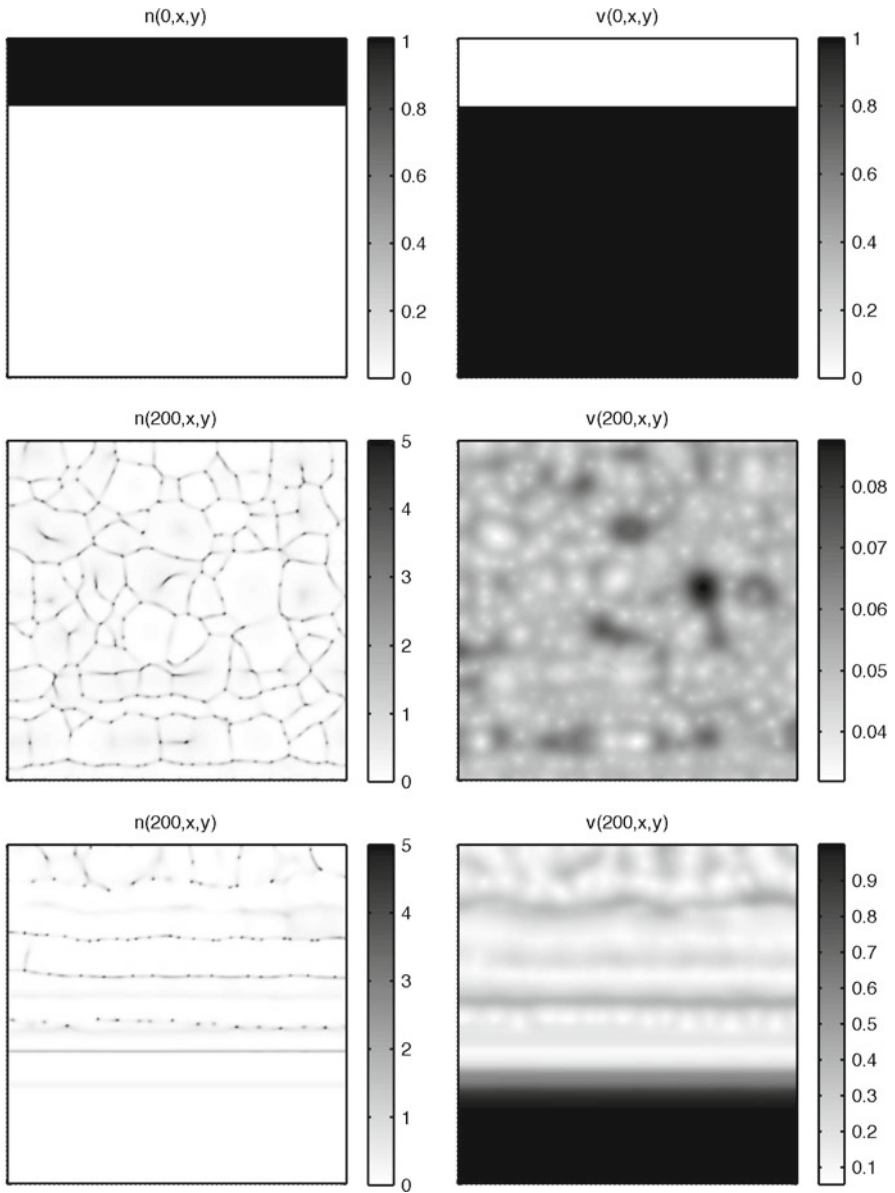
is formulated in terms of cancer cell invasion of ECM envisaged *in vivo*, it is very difficult to obtain data from *in vivo* systems. Such *in vitro* experimental systems as the collagen:matrigel assay provide an important first step at a qualitative comparison with our model.

Figure 12 shows the results of cancer cell invasion *in vitro* using such an organotypic culture model. The figures show different penetration depths of the extracellular matrix by cancer cells of varying grade. In the top left figure, we have the result using normal cells. The remaining three figures (top right, bottom left and bottom right) show the results using cells isolated from varying grade of tumour i.e. of increasing malignancy. As can be seen from the figures, as the cancer cells increase in malignancy, the depth of penetration into the extracellular matrix increases as does the extent of fragmentation i.e. heterogeneity.

In Fig. 13, we present simulation results obtained using the finite volume code for the model (2) on the square domain  $\Omega = (0, 5)^2$  with no-flux boundary conditions. The two figures in the top plots show the initial conditions for the cancer cells and ECM—a strip of cancer cells (at a uniform initial density of 1) is placed along the top



**Fig. 12** Modelling tumour cell invasion *in vitro* using an organotypic culture model reveals the varying extent of tumour mass fragmentation and extracellular matrix penetration. The figures show the depth of penetration into the extracellular matrix and the degree of fragmentation (heterogeneity) of tumour cells of increasing malignancy. Normal cells (*top left* figure) or cells isolated from varying grade of tumour (*top right*, *bottom left* and *bottom right* figures respectively) were cultured in contact with an extracellular matrix populated with normal stromal cells over a 14 day period. The figures show H & E stained sections from the three-dimensional culture, highlighting epithelial cells (tumour and normal) forming a multi-layered epithelia with or without extracellular matrix invasion



**Fig. 13** Plots showing the distribution of the cancer cell density  $n(t, x, y)$  and ECM density  $v(t, x, y)$  in a square domain  $\Omega = (0, 5)^2$ . The *top plots* show the initial conditions, with cancer cells taking up one fifth of the domain (*top left*) and ECM occupying the rest of the domain (*top right*). The *middle plots* show the cancer cell (*left*) and ECM (*right*) densities at  $t = 200$  using parameter set  $\mathcal{P}$ . The cancer cells have invaded the ECM in a very heterogeneous (fragmented) manner and penetrated almost to the lower boundary. The *bottom plots* show the cancer cell (*left*) and ECM (*right*) densities at  $t = 200$  using a modified parameter set reflecting a less aggressive cancer cell phenotype— $D_n = 2.5 \cdot 10^{-4}$ ,  $\chi_v = 0.01425$ ,  $\mu_1 = 0.1$ ,  $\delta = 4.15$ ,  $\phi_{53} = 0.45$  (all other parameters unchanged from parameter set  $\mathcal{P}$ ). In this case, the cancer cells have penetrated the ECM to a lesser degree and there is less heterogeneity (fragmentation). These simulations qualitatively mirror the experimental results shown in Fig. 12

20% of the square domain (cf. Fig. 12) and the ECM takes up the remaining 80% of the domain. The initial conditions for uPA, PAI-1 and plasmin follow those in Eq. 3 of Sect. 3, i.e.,  $u(0, \mathbf{x}) = 0.5n(0, \mathbf{x})$ ,  $p(0, \mathbf{x}) = 0.05n(0, \mathbf{x})$ , and  $m(0, \mathbf{x}) = 0$ .

The middle plots of Fig. 13 show the simulation results for the cancer cells and ECM using parameter set  $\mathcal{P}$ . The left hand plot shows the distribution of cancer cells which have invaded most of the domain at  $t = 200$  and are heterogeneously distributed throughout i.e. a lot of fragmentation. The ECM distribution (right hand plot) is correspondingly fragmented and heterogeneous. These results may be compared with the experimental data for the most malignant cancer cells shown in Fig. 12, bottom right plot, where we observe a large degree of cancer cell invasion and ECM degradation and heterogeneity.

Finally, the bottom plots of Fig. 13 show the simulation results for the cancer cells and ECM using a modified parameter set, reflecting a less malignant cancer cell population i.e. the diffusion coefficient  $D_n = 2.5 \cdot 10^{-4}$ , haptotactic coefficient  $\chi_v = 0.01425$ , cell proliferation rate  $\mu_1 = 0.1$ , matrix degradation rate  $\delta = 4.15$ , and production of plasmin  $\phi_{53} = 0.45$ . The left hand plot shows the distribution of cancer cells at  $t = 200$ . In contrast with the middle plot, in this case the cancer cells have penetrated the ECM to a lesser degree and there is less heterogeneity (fragmentation). Correspondingly the ECM is less degraded. Once again, these results may be compared with the experimental data for the less malignant cancer cells shown in Fig. 12, bottom left plot, where we observe lesser cancer cell and ECM heterogeneity.

## 6 Discussion and conclusions

In this paper we have investigated, analytically and numerically, a mathematical model of cancer cell invasion of tissue (extracellular matrix) first presented in [Chaplain and Lolas \(2005\)](#). The biological focus of the model is the urokinase plasminogen activation (uPA) system but it is conceivable that similar results could be obtained by focusing on alternative matrix/protease dependent remodelling systems such as those associated with transforming growth factor- $\beta$  activation ([Jenkins 2008](#)). Our main contribution and finding is the observation of a very rich (“dynamic”) spatio-temporal heterogeneity of the solutions. The linear stability analysis and computational simulations suggest that this may be due to a taxis-driven instability of the spatially homogeneous, positive steady state of the model, cf. ([Keller and Segel 1970](#); [Pearce et al. 2007](#)) (although we have not proved this). This in turn, leads to a very interesting and challenging open question to understand fully these “merging and emerging” dynamics. Furthermore, in this paper we have shown that by varying key parameters of the model, the qualitative character of the solution—either of travelling-wave-like form or heterogeneous dynamics—can be changed. The prevalent character of the solution for a given parameter set can be predicted by examining dispersion relations (such as those shown in this paper) derived from a linear stability analysis of the system.

Examples of the two different “types” of invasion by cancer cells observed here can be seen not only using laboratory based experimental models of cancer cell invasion, but also directly in clinical samples and certainly have implications for cancer

treatment. In the case of “dynamic heterogeneity”, a surgical removal of the tumour is made considerably more complicated and difficult due to the dissemination of small and individual tumour cell clusters in the tissue space, i.e. a breakup of an initially compact tumour mass. Here the danger is that surgery leaves some of those tumour cell clusters behind which then are the starting point for a re-establishment of the disease or that this departure of cells from the primary tumour mass leads directly to metastasis (Lindemann et al. 1992; Izbicki et al. 1997).

In the second type of behaviour, the travelling-wave-like regime, the tumour mass remains compact and can be more easily recognised as a whole and removed as such by the surgeon. However, with the parameters considered here, the tumour is still growing in this regime. We also note that in this case, although the tumour remains as a compact mass, the distance penetrated into the tissue is greater (since the wave speed is greater cf. Fig. 6). One may draw the general conclusion that manipulation of the tumour microenvironment (Sutherland 1988; Anderson et al. 2006), for example through the oxygen/nutrient supply to the tumour (and with a subsequent effect on cancer cell proliferation, migration, and enzyme production), may have a major impact on invasion. Different tumour types may possess varying abilities to maintain growth in the absence of oxygen/nutrient supply and different tumour types may evolve the ability to vascularise and re-supply the growing tumour mass. Rapid tumour growth either in a dynamic heterogeneous or a traveling-wave-like manner has the potential to lead to further evolution of the tumour but it is metastasis, not proliferation which results in cancer mortality (Sporn 1996). The act of cells breaking out and leaving the primary tumour site remains the most deadly trait. The extent of invasion depth has long been correlated with poor prognosis (Breslow 1970) and laboratory modelling and measurement of invasion tend to describe data more similar to the dynamic heterogeneous regime of invasion as “more aggressive” (Nyström et al. 2005) and Fig. 12.

In terms of future work and model development, we note that the model considered in this paper has some limitations. Future work will deal with these and now we comment on these briefly.

In the original paper of Chaplain and Lolas (2005) an additional proliferation term  $+\phi_{13}nu$  is present in the cancer cell equation of the model but is not considered here. This term models additional cancer cell proliferation as a result of signal pathways that are activated by uPA/uPAR binding. Such a dependence could be included in the model by allowing the cancer cell proliferation rate  $\mu_1$  to depend on the uPA concentration  $u$ . Other effects of the uPA system which are observed biologically will also be considered for inclusion in the model. This critical review is expected to lead to a more focused/streamlined model of the kinetics. Other extensions of the present model would be to include explicitly an equation for oxygen/nutrient supply to the cancer cells (Sherratt and Chaplain 2001) and to account in detail for effects of both cell–cell and cell–matrix adhesion. Although this effect has been modelled previously using discrete techniques (Anderson 2005; Turner and Sherratt 2002), an interesting approach using PDEs and continuum models has recently been developed by Gerisch and Chaplain (2008) building on initial work of Armstrong et al. (2006). In this approach, non-local terms in the PDE system are used to model the cell–cell and cell–matrix interactions, resulting in a system of integro-differential equations (Gerisch and Chaplain 2008; Painter et al. 2010).

Using this refined approach, coupled with accurate parameter estimation, it should be possible to develop a mathematical model of cancer invasion that assesses invasion objectively and provides a numerical “Invasion Index” (Nyström et al. 2005; Martins et al. 2009). The simulations presented in Fig. 13 show that such a mathematical model can provide information regarding both the depth and pattern of invasion, two key features of cancer cell invasion. By varying parameter values, the mathematical model is capable of indicating how various factors influence invasion. Future work in this direction will require a careful estimate of parameter values in the collagen:matrigel assay and a more detailed experimental investigation of the biochemical processes involving the matrix degrading enzymes.

Finally, we note that since cancer is a progressive disease (Hanahan and Weinberg 2000; MacSween 2003), with the cancer becoming more malignant as the cancer cells undergo successive mutations, an interesting development of the model would be to reflect this important aspect by introducing a “mutation pathway” into the model at a phenotypic level, whereby different sub-populations of increasingly malignant cells appear over time, cf. Spemulli and Dexter (1983); Heppner (1984); Enderling et al. (2007). An indication of how a model of this type with two cancer cell sub-populations, having densities  $n_1$  and  $n_2$ , respectively, might be implemented is given below:

$$\begin{aligned} \partial_t n_1 = & \underbrace{D_{n_1} \Delta n_1}_{\text{random motility}} - \nabla \cdot \left[ \underbrace{\chi_{u1} n_1 \nabla u}_{\text{uPA-chemo}} + \underbrace{\chi_{p1} n_1 \nabla p}_{\text{PAI-1-chemo}} + \underbrace{\chi_{v1} n_1 \nabla v}_{\text{VN-hapto}} \right] \\ & + \underbrace{\mu_{1,1} n_1 (1 - n)}_{\text{proliferation}} - \underbrace{\lambda n_1 F(t, v)}_{\text{conversion to } n_2}, \end{aligned} \tag{9a}$$

$$\begin{aligned} \partial_t n_2 = & \underbrace{D_{n_2} \Delta n_2}_{\text{random motility}} - \nabla \cdot \left[ \underbrace{\chi_{u2} n_2 \nabla u}_{\text{uPA-chemo}} + \underbrace{\chi_{p2} n_2 \nabla p}_{\text{PAI-1-chemo}} + \underbrace{\chi_{v2} n_2 \nabla v}_{\text{VN-hapto}} \right] \\ & + \underbrace{\mu_{1,2} n_2 (1 - n)}_{\text{proliferation}} + \underbrace{\lambda n_1 F(t, v)}_{\text{conversion from } n_1}, \end{aligned} \tag{9b}$$

where  $n$  denotes the total cell density,  $n := n_1 + n_2$ , and the conversion function  $F$  is a product of two Heaviside functions,

$$F(t, v) = H(t - 50) \cdot H(v - 0.3).$$

In the above model, we have assumed that the cancer cells of sub-population 1 are converted into cancer cells of sub-population 2 after  $t = 50$  and only in regions with sufficiently high ECM density  $v > 0.3$ . The differences between the two sub-populations are (1) in the diffusion coefficients—cancer cells of sub-population 2 diffuse faster than cancer cells of sub-population 1, i.e.  $D_{n_2} > D_{n_1}$ , (2) in the proliferation rates—cells of sub-population 2 proliferate more rapidly than cells of sub-population 1, i.e.  $\mu_{1,2} > \mu_{1,1}$ , (3) in the chemotactic and haptotactic constants—more aggressive cancer cells migrate more quickly i.e.  $\chi_{u2} > \chi_{u1}$ ,  $\chi_{up} > \chi_{p1}$ ,  $\chi_{v2} > \chi_{v1}$ . The other equations for the ECM, uPA, PAI-1, and plasmin remain unchanged from system (2).

Figure 14 shows the results of a computational simulation of the above 2 equations along with the uPA-system equations from model (2) using new values of the following parameters, we refer to as parameter set  $\mathcal{P}^*$

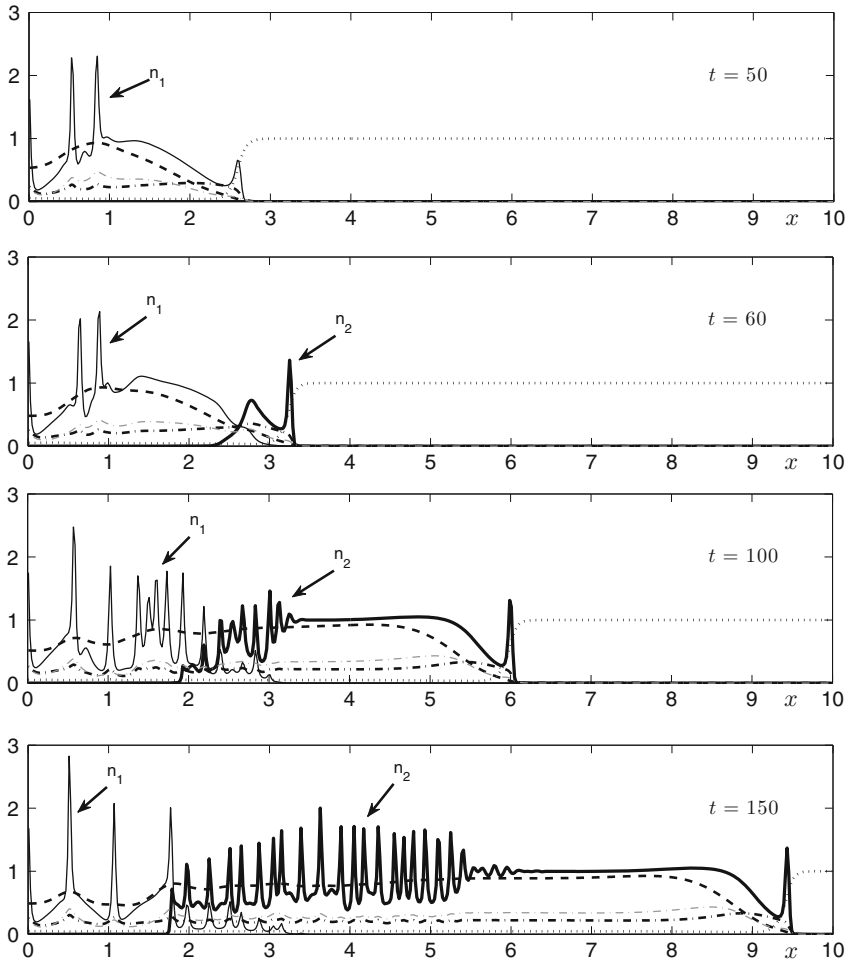


**Fig. 14** Plots showing the spatio-temporal evolution of the solution profiles of all variables of our extended model with two sub-populations of cancer cells  $n_1$  and  $n_2$ . Solution profiles are shown for times  $t = 50, 60, 100,$  and  $150$  using parameter set  $\mathcal{P}^*$ . The density of cancer cells of sub-population 1 is denoted by the *solid thin black line*, the density of the more aggressive cancer cells of sub-population 2 by the *solid thick black line*, the ECM density by the *dotted black line*, the uPA concentration by the *dash-dotted black line*, PAI-1 concentration by the *dashed black line*, and plasmin concentration by the *dash-dotted grey thin line*

$$\begin{aligned}
 D_{n_1} &= 3.5 \cdot 10^{-4}, & D_{n_2} &= 2.5 \cdot 10^{-4}, \\
 \mu_{1,1} &= 0.25, & \mu_{1,2} &= 0.75, \\
 \chi_{u1} &= 2.05 \cdot 10^{-2}, & \chi_{u2} &= 3.05 \cdot 10^{-2}, \\
 \chi_{p1} &= 2.75 \cdot 10^{-2}, & \chi_{p2} &= 3.75 \cdot 10^{-2}, \\
 \chi_{v1} &= 1.85 \cdot 10^{-2}, & \chi_{v2} &= 2.85 \cdot 10^{-2}, \\
 \lambda &= 0.3,
 \end{aligned}$$

and the rest of parameter values remains the same as parameter set  $\mathcal{P}$  given in Sect. 3.

As is to be expected, for  $t < 50$  the solutions evolve as in Fig. 14, first plot. After  $t = 50$  there is some conversion from sub-population 1 to sub-population 2 at the leading edge of the invading front and so by  $t = 60$  cancer cells of sub-population 2 are visible (second plot). As time increases, the more aggressive sub-population 2 gradually replaces the less aggressive sub-population (third and fourth plots). Furthermore, we observe an increase in the speed of invasion of the ECM by the more aggressive sub-population 2.

The results of the proposed model extension shown above indicate the potential for predicting the spatio-temporal evolution of an invasive cancer consisting of several heterogeneous sub-populations that differ in many phenotypic characteristics. Clinically, the different sub-populations within a primary tumour may give an impact on the design of treatment protocols to predict individual chemotherapy for cancer patients (Spremulli and Dexter 1983).

The ability to model different phenotypes of varying degrees of malignancy as well as cell–cell and cell–matrix adhesion at a continuum level, offers a fruitful future for a deeper understanding of the processes involved in cancer cell invasion and of their relative importance to each other. Although the present model and its proposed extension/development provides a suitable level of sophistication and complexity to discuss important features of cancer cell invasion, there are still many other known processes that we do not explicitly account for, such as genetic mutations and signal transduction pathways. Incorporation of such intracellular and genetic events in a genuine multi-scale model is the next big challenge appearing on the modelling horizon.

**Acknowledgments** MAJC gratefully acknowledges the support of ERC (European Research Council) AdG Grant No. 227619 “From Mutations to Metastases: Multiscale Mathematical Modelling of Cancer Growth and Spread”. VA was supported by an NRP (Northern Research Partnership) PhD Studentship.

## References

- Adam JA, Bellomo N (1996) A survey of models for tumour-immune system dynamics. Birkhäuser, Boston
- Aida M, Tsujikawa T, Efendiev M, Yagi A, Mimura M (2006) Lower estimates of the attractor dimension for a chemotaxis growth system. *J Lond Math Soc* 74:453–474
- Anderson ARA (2005) A hybrid mathematical model of solid tumour invasion: the importance of cell adhesion. *IMA Math Med Biol* 22(2):163–186. doi:[10.1093/imammb/dqi005](https://doi.org/10.1093/imammb/dqi005)
- Anderson ARA, Chaplain MAJ, Newman EL, Steele RJC, Thompson AM (2000) Mathematical modelling of tumour invasion and metastasis. *Comput Math Method M* 2(2):129–154
- Anderson ARA, Weaver AM, Cummings PT, Quaranta V (2006) Tumor morphology and phenotypic evolution driven by selective pressure from the microenvironment. *Cell* 127:905–915
- Anderson ARA, Rejniak KA, Gerlee P, Quaranta V (2009) Microenvironment driven invasion: a multiscale multimodel investigation. *J Math Biol* 58:579–624
- Andreassen PA, Kjølner L, Christensen L, Duffy MJ (1997) The urokinase-type plasminogen activator system in cancer metastasis: a review. *Int J Cancer* 72(1):1–22
- Andreassen PA, Egelund R, Petersen HH (2000) The plasminogen activation system in tumor growth, invasion, and metastasis. *Cell Mol Life Sci* 57(1):25–40. doi:[10.1007/s000180050497](https://doi.org/10.1007/s000180050497)
- Araujo RP, McElwain DLS (2004) A history of the study of solid tumour growth: the contribution of mathematical modelling. *B Math Biol* 66(5):1039–1091. doi:[10.1016/j.bulm.2003.11.002](https://doi.org/10.1016/j.bulm.2003.11.002)
- Armstrong NJ, Painter KJ, Sherratt JA (2006) A continuum approach to modelling cell–cell adhesion. *J Theor Biol* 243(1):98–113. doi:[10.1016/j.jtbi.2006.05.030](https://doi.org/10.1016/j.jtbi.2006.05.030)
- Bellomo N, Bellouquid A, De Angelis A (2003) The modelling of the immune competition by generalized kinetic (Boltzmann) models: Review and research perspectives. *Math Comput Model* 37:1131–1142

- Bellomo N, Chaplain MAJ, De Angelis E (2008) Selected topics in cancer modeling: genesis, evolution, immune competition, and therapy (Modeling and simulation in science, engineering and technology). Birkhäuser, Boston
- Breslow A (1970) Thickness, cross-sectional areas and depth of invasion in the prognosis of cutaneous melanoma. *Ann Surg* 172(5):902–908
- Byrne HM, Chaplain MAJ, Pettet GJ, McElwain DLS (2001) An analysis of a mathematical model of trophoblast invasion. *Appl Math Lett* 14(8):1005–1010
- Chaplain MAJ, Lolas G (2005) Mathematical modelling of cancer cell invasion of tissue: The role of the urokinase plasminogen activation system. *Math Mod Methods Appl Sci* 15:1685–1734
- Chaplain MAJ, Lolas G (2006) Mathematical modelling of cancer invasion of tissue: dynamic heterogeneity. *Net Hetero Med* 1:399–439
- Enderling H, Chaplain MAJ, Anderson ARA, Vaidya J (2007) A mathematical model of breast cancer development, local treatment and recurrence. *J Theor Biol* 246:245–259
- Folkman J (1974) Tumor angiogenesis. *Adv Cancer Res* 19:331–358
- Folkman J (1976) The vascularization of tumors. *Sci Am* 234(5):58–73
- Folkman J, Klagsbrun M (1987) Angiogenic factors. *Science* 235(4787):442–447
- Frieboes HB, Zheng X, Sun CH, Tromberg B, Gatenby R, Cristini V (2006) An integrated computational/experimental model of tumor invasion. *Cancer Res* 66:1597–1604
- Gatenby RA (1995) Models of tumor-host interaction as competing populations: implications for tumor biology and treatment. *J Theor Biol* 176(4):447–455. doi:[10.1006/jtbi.1995.0212](https://doi.org/10.1006/jtbi.1995.0212)
- Gatenby RA, Gawlinski ET (1996) A reaction-diffusion model of cancer invasion. *Cancer Res* 56(24):5745–5753
- Gerisch A, Chaplain MAJ (2006) Robust numerical methods for taxis–diffusion–reaction systems: Applications to biomedical problems. *Math Comput Model* 43:49–75
- Gerisch A, Chaplain MAJ (2008) Mathematical modelling of cancer cell invasion of tissue: local and non-local models and the effect of adhesion. *J Theor Biol* 250(4):684–704
- Hanahan D, Weinberg RA (2000) The hallmark of cancer. *Cell* 100:57–70
- Heppner GH (1984) Tumor heterogeneity. *Cancer Res* 44:2259–2265
- Hillen T (2006)  $M^2$  Mesoscopic and Macroscopic Models for Mesenchymal Motion. *J Math Biol* 53(4):585–616
- Hillen T, Painter KJ (2001) Global existence for a parabolic chemotaxis model with prevention of overcrowding. *Adv Appl Math* 26(4):280–301. doi:[10.1006/aama.2001.0721](https://doi.org/10.1006/aama.2001.0721)
- Hillen T, Painter KJ (2009) A user's guide to PDE models for chemotaxis. *J Math Biol* 58:183–217. doi:[10.1007/s00285-008-0201-3](https://doi.org/10.1007/s00285-008-0201-3)
- Horváth Z (1998) Positivity of Runge–Kutta and diagonally split Runge–Kutta methods. *Appl Numer Math* 28(2–4):309–326
- Izbicki JR, Hosch SB, Pichlmeier U, Rehders A, Busch C, Niendorf A, Passlick B, Broelsch CE, Pantel K (1997) Prognostic Value of Immunohistochemically Identifiable Tumor Cells in Lymph Nodes of Patients with Completely Resected Esophageal Cancer. *N Engl J Med* 337:1188–1194
- Jenkins G (2008) The role of proteases in transforming growth factor- $\beta$  activation. *Int J Biochem Cell Biol* 40(6–7):1068–1078. doi:[10.1016/j.biocel.2007.11.026](https://doi.org/10.1016/j.biocel.2007.11.026)
- Keller EF, Segel LA (1970) Initiation of slime mold aggregation viewed as instability. *J Theor Biol* 26:399–417
- Lindemann F, Schlimok G, Dirschedl P, Witte J, Riethmüller G (1992) Prognostic significance of micro-metastatic tumour cells in bone marrow of colorectal cancer patients. *Lancet* 340:685–689. doi:[10.1016/0140-6736\(92\)92230-D](https://doi.org/10.1016/0140-6736(92)92230-D)
- Lowengrub JS, Frieboes HB, Jin F, Chuang Y-L, Li X, Macklin P, Wise SM, Cristini V (2010) Nonlinear modelling of cancer: bridging the gap between cells and tumours. *Nonlinearity* 23:R1–R91. doi:[10.1088/0951-7715/23/1/R01](https://doi.org/10.1088/0951-7715/23/1/R01)
- MacSween RNM (2003) Muir's textbook of pathology. 14th edn. Arnold, London
- Mantzaris NV, Webb S, Othmer HG (2004) Mathematical modeling of tumor-induced angiogenesis. *J Math Biol* 49(2):111–187. doi:[10.1007/s00285-003-0262-2](https://doi.org/10.1007/s00285-003-0262-2)
- Martins VL, Vyas JJ, Chen M, Purdie K, Mein CA, South AP, McGrath JA and O'Toole EA (2009) Increased invasive behaviour in cutaneous squamous cell carcinoma with loss of basement-membrane type VII collagen. *J Cell Sci* 122:1788–1799. doi:[10.1242/jcs.042895](https://doi.org/10.1242/jcs.042895)
- Matzavinos A, Chaplain MAJ (2004) Travelling-wave analysis of a model of the immune response to cancer. *C R Biol* 327(11):995–1008

- Matzavinos A, Chaplain MAJ, Kuznetsov VA (2004) Mathematical modelling of the spatio-temporal response of cytotoxic T-lymphocytes to a solid tumour. *IMA J Math Med Biol* 21(1):1–34
- Nyström ML, Thomas GJ, Stone M, Mackenzie IC, Hart IR, Marshall JF (2005) Development of a quantitative method to analyse tumour cell invasion in organotypic culture. *J Pathol* 205(4):468–475. doi:[10.1002/path.1716](https://doi.org/10.1002/path.1716)
- Orme ME, Chaplain MAJ (1996) A mathematical model of the first steps of tumour-related angiogenesis: Capillary sprout formation and secondary branching. *IMA J Math Med Biol* 13:73–98
- Painter KJ (2009) Modelling cell migration strategies in the extracellular matrix. *J Math Biol* 58(4–5):511–543. doi:[10.1007/s00285-008-0217-8](https://doi.org/10.1007/s00285-008-0217-8)
- Painter KJ, Hillen T (2002) Volume-filling and quorum-sensing in models for chemosensitive movement. *Can Appl Math Q* 10(4):501–543
- Painter KJ, Armstrong NA, Sherratt JA (2010) The impact of adhesion on cellular invasion processes in cancer and development. *J Theor Biol* 264:1057–1067
- Parsons SL, Watson SA, Brown PD, Collins HM, Steele RJ (1997) Matrix metalloproteinases. *Br J Surg* 84(2):160–166
- Pearce IG, Chaplain MAJ, Schofield PG, Anderson ARA, Hubbard SF (2007) Chemotaxis-induced spatio-temporal heterogeneity in multi-species host-parasitoid systems. *J Math Biol* 55:365–388
- Pepper MS (2001) Role of the matrix metalloproteinase and plasminogen activator-plasmin systems in angiogenesis. *Arterioscler Thromb Vasc Biol* 21(7):1104–1117
- Perentes JY, McKee TD, Ley CD, Mathiew H, Dawson M, Padera TP, Munn LL, Jain RK, Boucher Y (2009) In vivo imaging of extracellular matrix remodeling by tumor-associated fibroblasts. *Nature Methods* 6(2):143–145. doi:[10.1038/nmeth.1295](https://doi.org/10.1038/nmeth.1295)
- Perumpanani AJ, Sherratt JA, Norbury J, Byrne HM (1996) Biological inferences from a mathematical model for malignant invasion. *Invasion Metastasis* 16(4–5):209–221
- Perumpanani AJ, Simmons DL, Gearing AJH, Miller KM, Ward G, Norbury J, Schneemann M, Sherratt JA (1998) Extracellular matrix-mediated chemotaxis can impede cell migration. *Proc Roy Soc Lond B* 265:2347–2352
- Poplawski NJ, Agero U, Gens JS, Swat M, Glazier JA, Anderson ARA (2009) Front instabilities and invasiveness of simulated avascular tumors. *Bull Math Biol* 71:1189–1227
- Preziosi L (ed) (2003) Cancer modelling and simulation. Chapman & Hall/CRC Press, Boca Raton
- Ramis-Conde I, Drasdo D, Anderson ARA, Chaplain MAJ (2008) Modeling the influence of the E-cadherin-*beta*-catenin pathway in cancer cell invasion: a multiscale approach. *Biophys J* 95:155–165. doi:[10.1529/biophysj.107.114678](https://doi.org/10.1529/biophysj.107.114678)
- Sherratt JA, Chaplain MAJ (2001) A new mathematical model for avascular tumour growth. *J Math Biol* 43:291–312
- Sporn MB (1996) The war on cancer. *Lancet* 347(9012):1377–1381
- Spremluli EN, Dexter DL (1983) Human tumor cell heterogeneity and metastasis. *J Clin Oncol* 1(8):496–509
- Sutherland RM (1988) Cell and environment interactions in tumor microregions: the multicell spheroid model. *Science* 240:177–184
- Szymańska Z (2003) Analysis of immunotherapy models in the context of cancer dynamics. *Int J Appl Math Comp* 13:407–418
- Szymańska Z, Rodrigo CM, Lachowicz M, Chaplain MAJ (2009) Mathematical modelling of cancer invasion of tissue: the role and effect of nonlocal interactions. *Math Mod Methods Appl Sci* 19(2):257–281
- Turner S, Sherratt JA (2002) Intercellular adhesion and cancer invasion: a discrete simulation using the extended Potts model. *J Theor Biol* 216(1):85–100. doi:[10.1006/jtbi.2001.2522](https://doi.org/10.1006/jtbi.2001.2522)
- Wang Z, Hillen T (2007) Classical solutions and pattern formation for a volume filling chemotaxis model. *Chaos* 17:037108. doi:[10.1063/1.2766864](https://doi.org/10.1063/1.2766864)
- Weiner R, Schmitt BA, Podhaisky H (1997) ROWMAP—a ROW-code with Krylov techniques for large stiff ODEs. *Appl Numer Math* 25:303–319